J. Fluid Mech. (2016), *vol.* 800, *pp.* 613–644. © Cambridge University Press 2016
doi:10.1017/jfm.2016.404

Reynolds stress distribution and turbulence generated secondary flow in the turbulent three-dimensional wall jet

L. Namgyal[1,†] and J. W. Hall[1]

[1]Department of Mechanical Engineering, University of New Brunswick, Fredericton, E3B 5A3, Canada

(Received 29 October 2015; revised 30 May 2016; accepted 10 June 2016;
first published online 13 July 2016)

The lateral half-width of the turbulent three-dimensional wall jet is typically five to eight times larger than the vertical half-width normal to the wall. Although the reason for this behaviour is not fully understood, it is caused by mean secondary flows that develop in the jet due to the presence of the wall. The origin of the secondary flow has been associated previously with both vorticity reorientation and also gradients in the Reynolds stresses, although this has not been directly quantified as yet. The present investigation focuses on a wall jet formed using a circular contoured nozzle with exit Reynolds number of 250 000. Stereoscopic particle image velocimetry measurements are used herein to measure the three-component velocity, thereby allowing access to the full Reynolds stress tensor that contributes to the secondary flow in a turbulent three-dimensional wall jet. Throughout the jet, the Reynolds normal stress ($\overline{u^2}$) makes the largest contribution to the Reynolds stress field whereas Reynolds shear stress ($\overline{vw}$) is found to be negligible when compared with other stresses. In particular, the differences in the Reynolds normal stresses ($\overline{v^2} - \overline{w^2}$) are found to be significantly larger than $\overline{vw}$; these terms are important for the generation of turbulence secondary flow in the wall jet. Above all, the differences in the Reynolds normal stresses are oriented to reinforce the near-wall streamwise vorticity, and thus contribute to the large lateral growth of this flow. The contours of the turbulent kinetic budget indicate that the turbulent energy budget obtained on the jet centreline is different from that obtained off of the jet centreline.

Key words: turbulent flows

1. Introduction

Three-dimensional wall jets are formed when a fluid flows from a finite width opening tangentially along a wall, as shown in figure 1. Wall jets have a diverse range of engineering applications, among which are included the cooling of gas turbine combustor walls, ventilation systems, and flow under dam sluice gates and over spillways. The three-dimensional wall jet is normally characterized by taking profiles along the jet centreline and across the jet at y_{max}, the height of the maximum velocity point, U_{max} (as shown in figure 1*a*). One of the most noteworthy features of

† Email address for correspondence: namgyaling@gmail.com

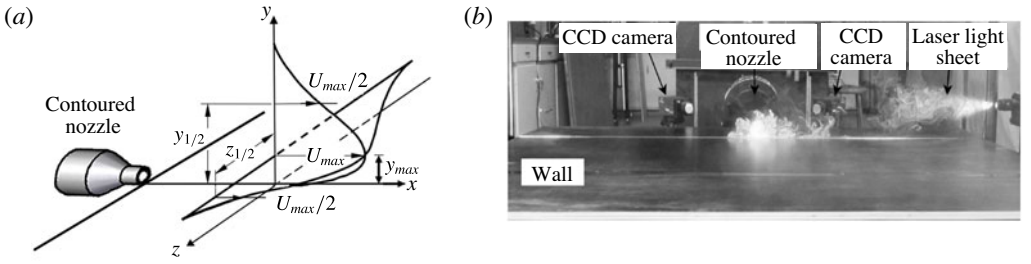

FIGURE 1. (*a*) Schematic and nomenclature for a three-dimensional wall and (*b*) experimental set-up showing the laser and PIV camera arrangement.

a three-dimensional wall jet is that the growth of the lateral half-width is five to eight times greater than the vertical half-width in the far field (e.g. Davis & Winarto 1980; Launder & Rodi 1983; Padmanabham & Gowda 1991*a*,*b*; Abrahamsson, Johansson & Lofdahl 1997*b*; Venas *et al.* 1999; Craft & Launder 2001; Sun 2002; Sun & Ewing 2002*b*; Hall & Ewing 2007*b*; Agelinchaab & Tachie 2011; Namgyal 2012).

The cause of the large lateral growth of turbulent three-dimensional wall jets is not fully understood; Launder & Rodi (1983) noted that the large lateral growth had to be related to mean secondary flows in the jet, and examined the governing equations for the transport of mean streamwise vorticity for steady incompressible flow:

$$\underbrace{\frac{\mathrm{D}\overline{\Omega}_x}{\mathrm{D}t}}_{A} = \underbrace{\overline{\Omega}_x\frac{\partial \overline{U}}{\partial x}}_{B} + \underbrace{\overline{\Omega}_y\frac{\partial \overline{U}}{\partial y} + \overline{\Omega}_z\frac{\partial \overline{U}}{\partial z}}_{C} + \underbrace{\frac{\partial^2}{\partial y\partial z}(\overline{v^2}-\overline{w^2})}_{D} + \underbrace{\left(\frac{\partial^2}{\partial z^2}-\frac{\partial^2}{\partial y^2}\right)\overline{vw}}_{E} + \underbrace{\nu\left(\frac{\partial^2\Omega_x}{\partial x^2}+\frac{\partial^2\overline{\Omega}_x}{\partial y^2}+\frac{\partial^2\overline{\Omega}_x}{\partial z^2}\right)}_{F}, \tag{1.1}$$

where A is the transport of streamwise vorticity; B is the streamwise amplification of mean vorticity by vortex stretching; C is the vorticity production by vortex-line bending; D is the vorticity production by gradients in the cross-flow Reynolds normal stresses; E is the vorticity production by gradients in the cross-flow Reynolds shear stress; F is the viscous diffusion of vorticity; $\overline{\Omega_x}$ is the mean streamwise vorticity; $\overline{\Omega_y}$ is the mean normal vorticity; $\overline{\Omega_z}$ is the mean lateral vorticity; $\overline{u^2}$, $\overline{v^2}$ and $\overline{w^2}$ are the Reynolds normal stress; $\overline{vw}$ is the Reynolds shear stress; $\overline{U}$ is the mean streamwise velocity; ν is the kinematic viscosity; x is the streamwise coordinate; y is the vertical coordinate; and z is the lateral coordinate.

Launder & Rodi (1983) stated that one possible source of streamwise vorticity in the three-dimensional wall jet was due to the vortex-line bending (term C). They suggested that this causes the formation of the two counter-rotating regions of mean streamwise vorticity on either side of the jet centreline in the far field. These regions were thought to drive the mean flow down towards the wall and eject it laterally outward, thereby causing the large lateral spreading. Many experimental studies have found evidence of mean streamwise vorticity like that proposed by Launder & Rodi (1983), although, in general, the oppositely signed regions of mean streamwise vorticity on either side of the jet centreline have tended to be side by side, as opposed to on top of one another (Matsuda, Iida & Hayakawa 1990; Sun & Ewing 2002*a*;

Hall & Ewing 2005*a*,*b*, 2006, 2007*a*, 2010; Namgyal & Hall 2011). These regions of mean streamwise vorticity have also tended to be closer to the wall than U_{max}, so the profiles measured across the jet at y_{max}, as typically done, would offer little information about the secondary flow.

Launder & Rodi (1983) also suggested that the mean streamwise vorticity could be generated because of gradients in the Reynolds stresses (terms D and E). They argued that the production of mean streamwise vorticity due to gradients in the normal stresses (term D) should be of the same order as the vortex-tilting terms and should act to reinforce the secondary flow due to vortex tilting in the far field. Later, Craft & Launder (2001) numerically examined the three-dimensional wall jet and noted that a similar vortex-tilting process should occur in the laminar jet to that in the turbulent case. They modelled the laminar jet and found that the lateral growth was significantly less than in the turbulent case. From this, they argued that the vortex-tilting process alone was not sufficient to cause the large lateral spreading that occurs in the turbulent wall jet, and thus it must be due to gradients in the Reynolds stresses.

Unfortunately, little information exists about the Reynolds stress distribution in the three-dimensional wall jet, in particular $\overline{vw}$, $\overline{v^2}$ and $\overline{w^2}$. Despite the widespread attention paid to the three-dimensional wall jet, there have been no previous investigations that have measured the full Reynolds stress tensor throughout the wall jet. Many studies have used hot-wire anemometry to examine the turbulent profiles on the jet centreline and at y_{max} (e.g. Davis & Winarto 1980; Padmanabham & Gowda 1991*a*,*b*; Abrahamsson *et al.* 1997*b*; Venas *et al.* 1999; Sun 2002; Sun & Ewing 2002*b*; Hall & Ewing 2007*b*); however, these studies did not measure all of the components of the Reynolds stress tensor. Particle image velocimetry has been used in the three-dimensional wall jet by Agelinchaab & Tachie (2011), although the measurements they presented were confined to the jet centreline or profiles at y_{max}. Full flow field measurements have been performed in the full cross-flow plane using hot-wire anemometry (Matsuda *et al.* 1990; Sun & Ewing 2002*b*; Hall & Ewing 2007*a*,*b*), but these measurements only measured the mean streamwise velocity or a few components of the Reynolds stress tensor.

In the present paper, stereoscopic PIV is used for computing these stresses to improve our understanding of the distribution of the Reynolds stresses and in turn the secondary flow in the three-dimensional wall jet.

2. Experimental set-up

The air flow to the jet was supplied by a 4.5 kW single-stage centrifugal blower. The flow was conditioned using a 0.9 m × 0.9 m × 0.9 m settling chamber which had three 10 mm screens. The flow from the settling chamber then passed through a flow straightener placed inside a 0.20 m diameter pipe. Finally, the air flowed through a contoured nozzle with an area ratio of 28 : 1 and a diameter of 38.1 mm. The nozzle had a fifth-order polynomial profile so as to yield a top-hat exit velocity profile with less than 0.25 % turbulence intensity. For all measurements, the jet Reynolds number at the outlet was set to 250 000. Upon exiting the nozzle the air flowed tangentially along a 2.49 m × 2.08 m horizontal wall forming the three-dimensional wall jet.

The velocity field was acquired using a LaVision Stereoscopic PIV system. Both the laser and the cameras were arranged as shown in figure 1(*b*). The flow and surrounding air were seeded using olive oil droplets generated by a Laskin type atomizer. This produced a mean particle diameter of 3 μm. A Solo 120XT Nd–Yag laser having a pulse energy of 120 mJ was used to illuminate the flow. The

x/D	Number of snapshots	$\overline{U}$ (%)	u (%)	$\overline{vw}$ (%)	$(\overline{v^2}-\overline{w^2})$ (%)
5	3000	0.14	3.41	3.70	3.17
10	3000	0.60	3.30	3.95	3.55
15	3000	0.74	3.62	4.31	4.13
20	4500	0.69	3.38	4.63	4.70
30	5100	0.71	3.09	5.16	4.92
40	6000	0.76	4.70	5.64	5.15

TABLE 1. Uncertainty in the estimators of $\overline{U}$, u, $\overline{vw}$ and $(\overline{v^2}-\overline{w^2})$ at 95 % confidence level (due to sampling time) at y_{max}.

images from the tracer particles were acquired by a pair of 12 bit CCD cameras (LaVision Imager Intense) with a resolution of 1376 × 1040 pixels. The double frame instantaneous images were processed using LaVision Flow Manager (DaVis 7.2 version). In the data processing, multi-pass decreasing interrogation window sizes from 64 × 64 pixels to 32 × 32 pixels with 75 % overlap were adopted and a normalized correlation function was used, and then the processed data were reconstructed using the Whittaker algorithm (Whittaker 1915; LaVision 2007).

In order to have statistically converged data, the following number of independent pairs of images were taken at various downstream locations; 3000 image pairs up to $x/D=15$, 4500 at $x/D=20$, 5100 at $x/D=30$ and 6000 at $x/D=40$. Only one half of the jet could be measured at $x/D=40$ due to limitations in the laser source, so statistics for one half of the jet were computed at this position. Since every vector field could be considered as an independent event due to the time lag between the image pairs, the uncertainties at 95 % confidence level associated with the mean streamwise velocity at the centre of the jet at y_{max} and at $y_{1/2}$ were determined to be within 0.14–0.76 % and 1.04–1.55 % respectively. The uncertainties in estimating $\overline{U}$ and some of the quantities of interest are also included in table 1.

3. Experimental results

The jet development can be characterized by examining the decay of the local maximum mean streamwise velocity, as shown in figure 2. The measurements are compared with those of Sun (2002) (contoured nozzle) and Hall & Ewing (2007*b*) (long channel). Here, U_{max} is normalized by the mean outlet velocity for the contoured nozzle jets and by the bulk velocity at the jet outlet for the channel jets. The x coordinate is normalized by D for the circular jets and $\sqrt{A}$ for the channel jets; this parameter was shown by Rajaratnam & Pani (1974) and Hall & Ewing (2007*b*) to collapse the streamwise development of three-dimensional wall jets issuing from non-circular channels.

At $x/D=5$, the local maximum velocity is still equal to the exit velocity. This indicates the persistence of the jet potential core at this location. Downstream at $x/D=10$, the mean velocity drops off considerably, showing that the collapse of the potential core has occurred by this point, which signifies the onset of the intermediate field. Further downstream, the jet velocity continues to decay due to the entrainment of ambient air, as expected. The present investigation shows reasonable agreement with Sun (2002), and the minor differences here can probably be attributed to the different jet Reynolds numbers. The local maximum streamwise velocity measured by Hall &

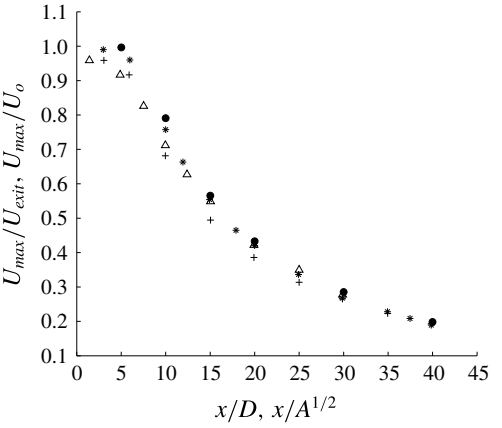

FIGURE 2. The decay of the local maximum streamwise velocity of the wall jet: (●) present investigation, (+) $A_r = 1$ and (△) $A_r = 4$ channel jets by Hall & Ewing (2007*b*), and (∗) contoured nozzle by Sun (2002).

Ewing (2007*b*) decays slightly faster than for the current results, in particular in the near-field region. This behaviour is due to the long channel exit condition used by Hall and Ewing, and the known slower development of channel jets compared with contoured nozzles (Hall & Ewing 2007*b*).

The development of the three-dimensional wall jet is next characterized by examining the streamwise variation of the vertical and lateral half-widths, as shown in figures 3(*a*) and 3(*b*) respectively. These results are compared with the half-widths measured by Sun & Ewing (2002*b*). The variations in the vertical half-width agree well with the data of Sun & Ewing (2002*b*), but the lateral half-widths measured here are slightly lower, particularly in the far-field region. A least-square linear fit of the vertical half-width yields a vertical growth rate of 0.041, which is close to the consensus value determined by Launder & Rodi (1983) (0.048). The streamwise variation of the normalized lateral half-width was not linear, so a fourth-order polynomial function was fitted to the data, as shown in figure 3(*b*). The lateral half-width determined in the region $30 \leqslant x/D \leqslant 40$ was 5.6 times the vertical half-width, agreeing with the value of 5.5 determined by Hall & Ewing (2007*b*) but slightly higher than the value reported by Sun & Ewing (2002*b*).

To set the context for the secondary flow and Reynolds stress results, all three components of the mean velocity field are examined in figures 4–6. All of the mean velocity contours are normalized by the local maximum streamwise velocity, U_{max}, and the respective jet half-width. A comparison of the streamwise evolution of the normalized mean streamwise velocity is shown at all downstream locations in figure 4. The contours indicate that the jet starts off round and that the lateral growth of the jet is observed to start near the wall. As the flow evolves downstream, the contours of the mean streamwise velocity begin to bulge more at the wall and begin to take on the characteristic wall jet shape, loosely approaching a self-similar shape at $x/D = 30$. These results are quite similar to contours of the mean flow acquired by Matsuda *et al.* (1990), Sun & Ewing (2002*b*) and Hall & Ewing (2007*a*).

As shown in figure 6, the bulging in the mean streamwise velocity near the wall is accompanied by large lateral velocities that persist near the wall on either side of

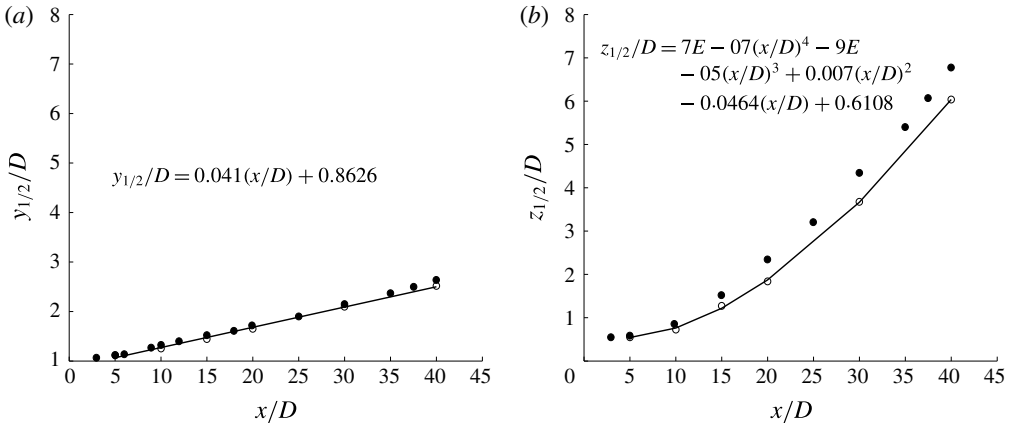

FIGURE 3. (*a*) The streamwise development of the vertical half-width in a three-dimensional wall jet: (○) present investigation, (●) Sun (2002) and (—) least-square linear fit. (*b*) The streamwise development of the lateral half-width in a three-dimensional wall jet: (○) present investigation, (●) Sun (2002) and (—) fourth-order polynomial fit.

the jet centreline (figure 6). Near the wall, these lateral velocities are oriented to eject flow laterally outward. The strength of the lateral flow relative to U_{max} increases as the jet evolves downstream, reaching approximately 14 % of U_{max}, which is consistent with the known increase in lateral growth as the jet develops from the near field to the far field (e.g. Sun 2002). It should also be noted that these large lateral velocities tend to be strongest below y_{max}, traversing in the z direction, and at this height would underestimate the mean lateral velocities.

The normalized contours of $\overline{V}$, shown in figure 5, also vary significantly as the jet evolves downstream. In the near field, at $x/D = 5$, the velocity at the centre of the jet is positive, indicating that the jet is on average growing away from the wall, whereas in the shear layers around the jet, the velocities are negative, indicating that the flow is directed downward. The negative velocities are probably associated with the downward entrainment of ambient air. The region of large negative velocity tends to grow and surround the small region of positive $\overline{V}$ as the flow evolves downstream, suggesting that as the jet develops downstream, the flow is overwhelmingly drawing the surrounding fluid down towards the wall. Taken together, the contours of $\overline{V}$ and $\overline{W}$ suggest that this downward mean flow probably supplies the strongly lateral outward mean flow.

Jet development is often characterized by examining the mass flow rate,

$$Q = \int_A \rho \overline{U}\, \mathrm{d}y\, \mathrm{d}z, \tag{3.1}$$

and momentum flux of the jet,

$$M = \int_A \rho \overline{U}^2\, \mathrm{d}y\, \mathrm{d}z. \tag{3.2}$$

These values have been determined in free jets by Panchapakesan & Lumley (1993), Hussein, Capp & George (1994) and Tinney, Glauser & Ukeiley (2008) but have never

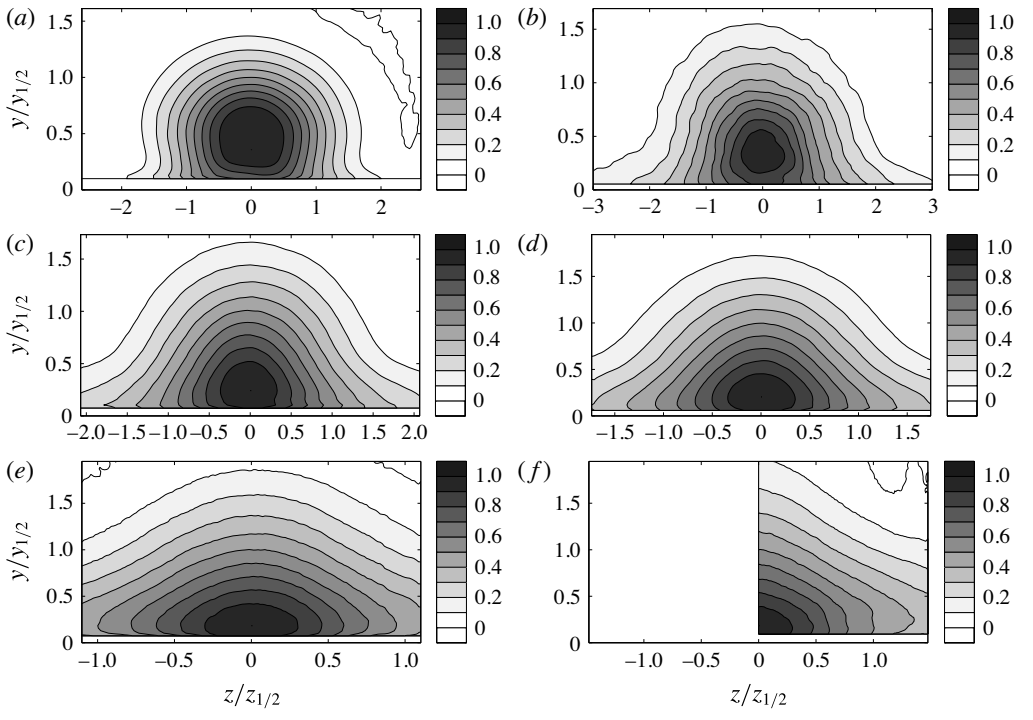

FIGURE 4. The normalized mean streamwise velocity, $\overline{U}/U_{max}$, at various downstream locations: (*a*) $x/D = 5$, (*b*) $x/D = 10$, (*c*) $x/D = 15$, (*d*) $x/D = 20$, (*e*) $x/D = 30$ and (*f*) $x/D = 40$.

been used in the three-dimensional wall jet, mostly due to a lack of high-density full flow field measurements like those here. The streamwise variation of the mass entrainment ratio, $(Q - Q_o)/Q_o$, is shown in figure 7(*a*), where Q_o is the mass flow rate at the nozzle outlet. The current results are compared with those in a free jet exiting from a round sharp-edged orifice (Quinn 2005). In both cases, the entrainment of air increases linearly with the downstream distance; however, the entrainment values for the wall jet are approximately one half of those for the free jet. This reduced entrainment is not unexpected because the presence of the wall reduces the surface area for which the jet can entrain ambient fluid.

The variation of the momentum flux ratio, M/M_o, where M_o is the outlet momentum flux, is shown in figure 7(*b*). For a free jet, it is well known that mean momentum is conserved throughout the jet (Capp, Hussien & George 1990; Hussein *et al.* 1994; Tinney *et al.* 2008), while here the momentum flux decreases as the jet evolves downstream. This is due to momentum being lost to the wall. This decrease is significantly larger than the momentum flux variation observed in a two-dimensional plane wall jet by Eriksson, Karlsson & Persson (1998). This can probably be attributed to the (obvious) enhanced three-dimensionality (and associated near-wall turbulence) of the present flow over a two-dimensional wall jet.

Profiles of the Reynolds stresses measured on the jet centreline are shown in figure 8. The results have been normalized by the square of the local maximum streamwise velocity, U_{max}^2, and $y_{1/2}$. At $x/D = 40$, the current Reynolds stress

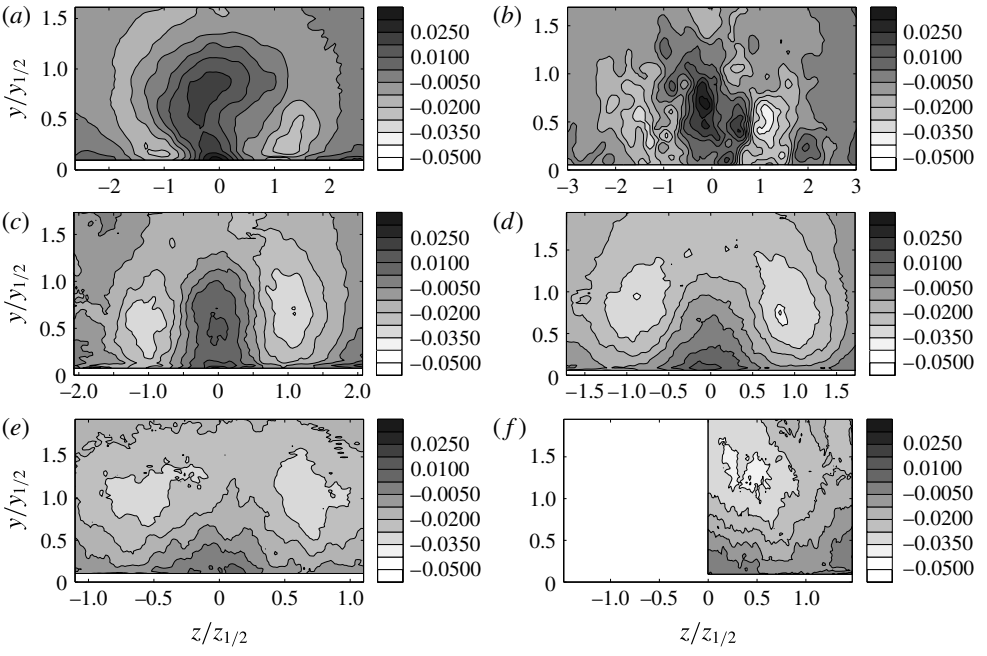

FIGURE 5. The normalized mean velocity normal to the wall, $\overline{V}/U_{max}$, at various downstream locations: (*a*) $x/D=5$, (*b*) $x/D=10$, (*c*) $x/D=15$, (*d*) $x/D=20$, (*e*) $x/D=30$ and (*f*) $x/D=40$.

measurements, $\overline{vv}$ and $\overline{uv}$, are compared with the results of Abrahamsson *et al.* (1997*b*) ($\overline{vv}$ and $\overline{uv}$) and Venas *et al.* (1999) ($\overline{uv}$). The results indicate good agreement with the present measurement near the wall, but show some differences in the outer regions. This is probably due to the known underprediction of conventional hot-wire measurements when the local turbulence intensity is high, like in the outer region of the wall jet. This underprediction of conventional hot-wire measurements in the outer region of both two- and three-dimensional wall jets has been previously discussed by Venas *et al.* (1999) and was also discussed by Namgyal & Hall (2010) in the three-dimensional wall jet measured using two-dimensional PIV.

Throughout the jet, $\overline{u^2}$ makes the largest contribution to the Reynolds stresses at all downstream positions; this is again due to the much larger value of $\overline{U}$ than $\overline{V}$ or $\overline{W}$ (Namgyal 2012). More details on the mean and fluctuating velocities can be found in Namgyal (2012). The profiles of the normal stresses, $\overline{v^2}$ and $\overline{w^2}$, at the jet centreline indicate that initially in the near-field region at $x/D=5$, $\overline{w^2}$ is dominant over $\overline{v^2}$, both near the wall and in the outer region around $y/y_{1/2}=0.8$ to 1.3 (figure 8*a*). However, as the flow progresses downstream, the magnitudes of both $\overline{v^2}$ and $\overline{w^2}$ become nearly equal in the outer region, while $\overline{w^2}$ still remains dominant over $\overline{v^2}$ in the region close to the wall (figure 8*e*,*f*). These results suggest that the near-wall anisotropy of the turbulence is not an artefact of the potential core, and seems to be characteristic of intermediate and far-field jet development.

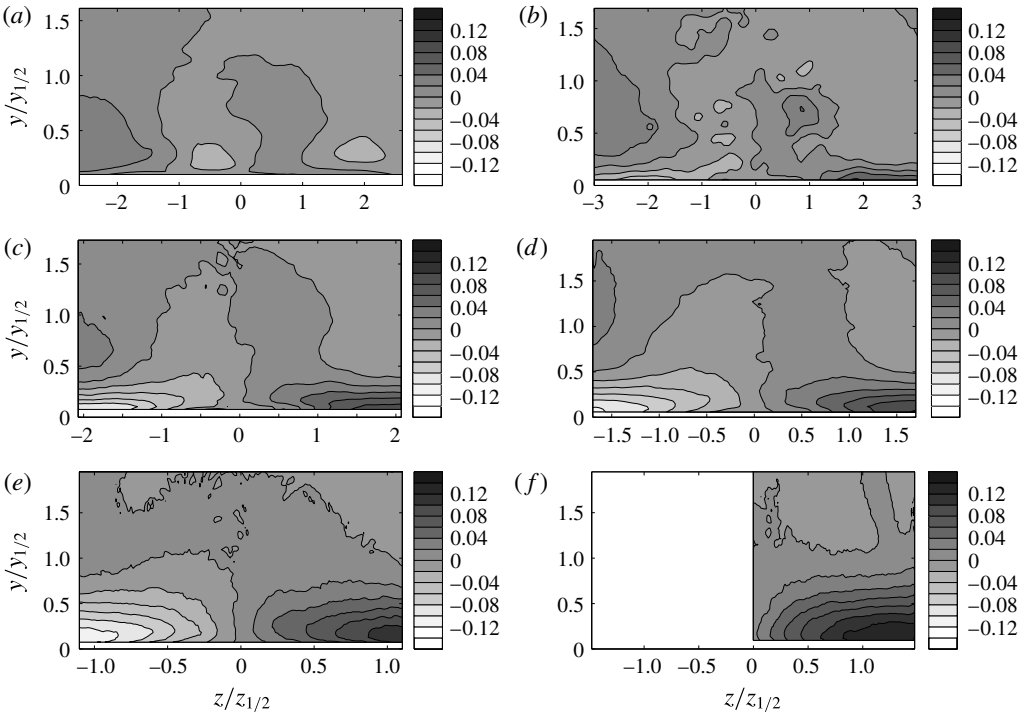

FIGURE 6. The normalized mean lateral velocity, $\overline{W}/U_{max}$, at various downstream locations: (*a*) $x/D = 5$, (*b*) $x/D = 10$, (*c*) $x/D = 15$, (*d*) $x/D = 20$, (*e*) $x/D = 30$ and (*f*) $x/D = 40$.

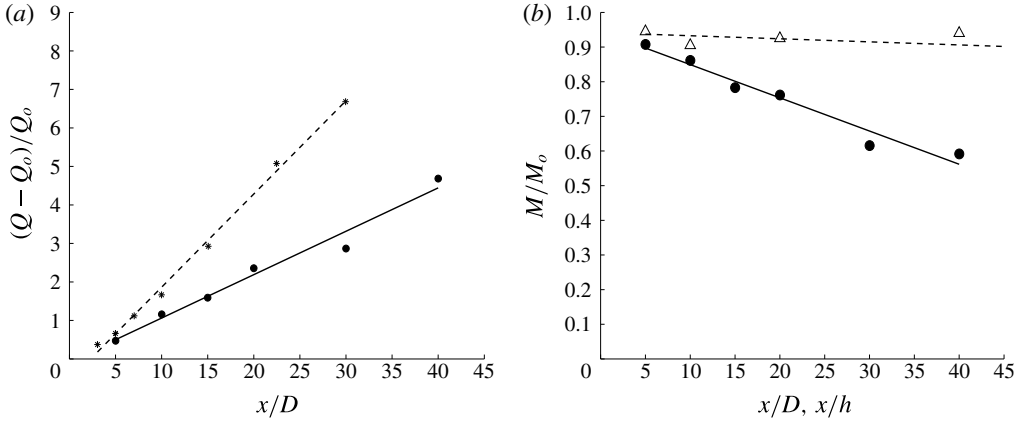

FIGURE 7. (*a*) Mass entrainment into the jet: (●) present investigation (contoured nozzle) and (∗) sharp-edged slot round jet by Quinn (2005). (*b*) Momentum flux of the jet: (●) present investigation and (△) two-dimensional plane wall jet by Eriksson *et al.* (1998).

At $x/D = 5$, the values of $\overline{uv}$ in the outer shear layer are comparable to $\overline{v^2}$ but are much larger than $\overline{vw}$ or $\overline{uw}$, whereas the values of $\overline{uv}$ are negative close to the wall in the inner shear layer. By $x/D = 15$, the negative near-wall peak in $\overline{uv}$ dissipates and the largest values of $\overline{uv}$ tend to occur in the outer shear layer at approximately $y/y_{1/2} = 0.8$ but get slightly lower as the jet evolves downstream to approximately

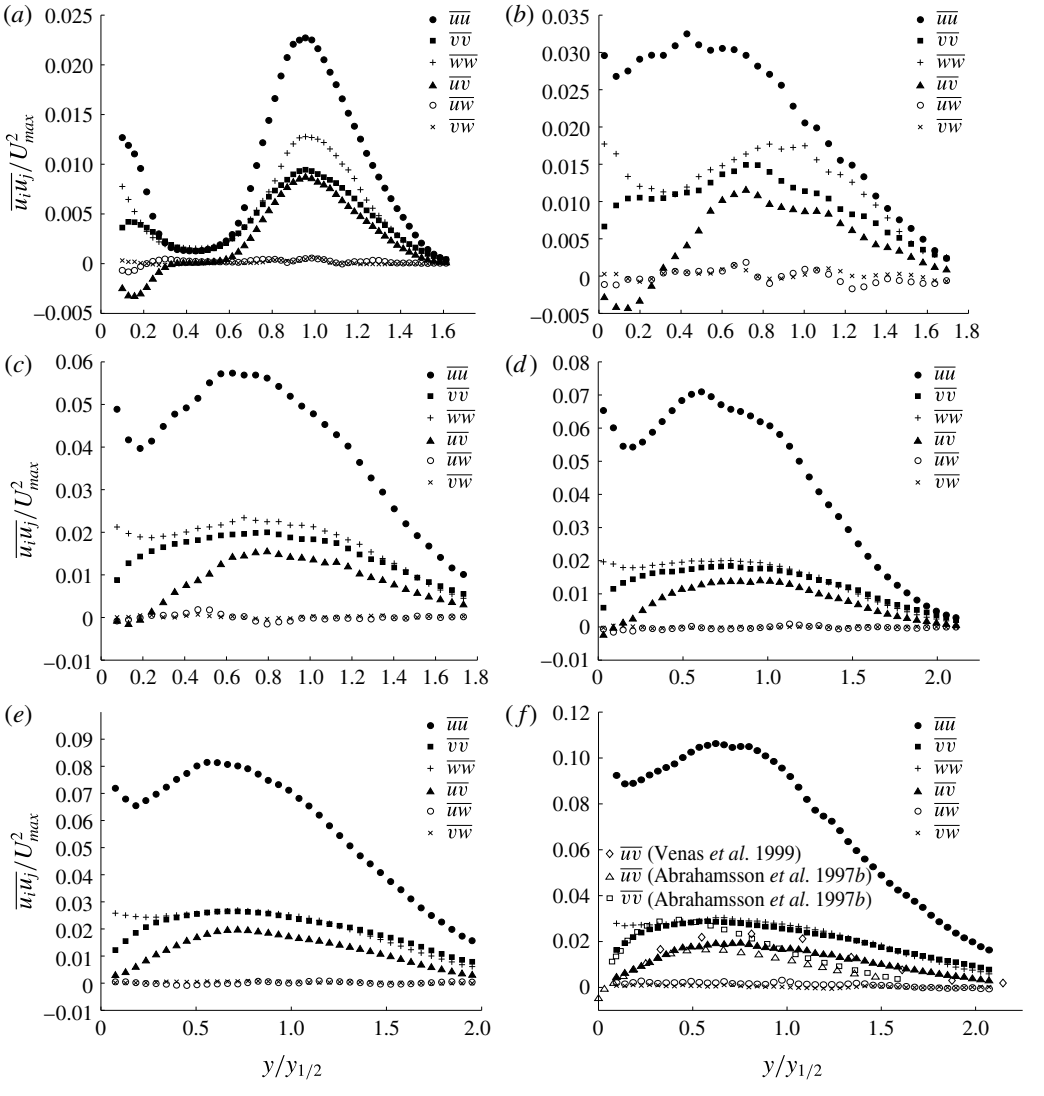

FIGURE 8. Profiles of the normalized Reynolds stresses measured at the jet centreline for various streamwise locations: (*a*) $x/D = 5$, (*b*) $x/D = 10$, (*c*) $x/D = 15$, (*d*) $x/D = 20$, (*e*) $x/D = 30$ and (*f*) $x/D = 40$; (●) $\overline{uu}$, (■) $\overline{vv}$, (□) $\overline{vv}$ (Abrahamsson *et al.* 1997*b*), (+) $\overline{ww}$, (▲) $\overline{uv}$, (△) $\overline{uv}$ (Abrahamsson *et al.* 1997*b*), (◇) $\overline{uv}$ (Venas *et al.* 1999), (○) $\overline{uw}$ and (×) $\overline{vw}$.

$y/y_{1/2} = 0.75$. This is in reasonable agreement with Sun (2002), who found that $\overline{uv}$ peaked at a height of approximately $y/y_{1/2} = 0.7$ by $x/D = 90$. Both the shear stresses, $\overline{uw}$ and $\overline{vw}$, are quite small compared with the other Reynolds stresses at the jet centreline at all streamwise locations. This is probably related to the negligible $\overline{W}$ values on the jet centreline.

The Reynolds stress profiles measured across the jet at y_{max} are shown in figure 9, normalized by $z_{1/2}$ and U_{max}^2. Initially, at $x/D = 5$, the Reynolds stresses are the largest at $z_{1/2}$ in the lateral shear layers. The relative magnitudes of $\overline{u^2}$ are the largest,

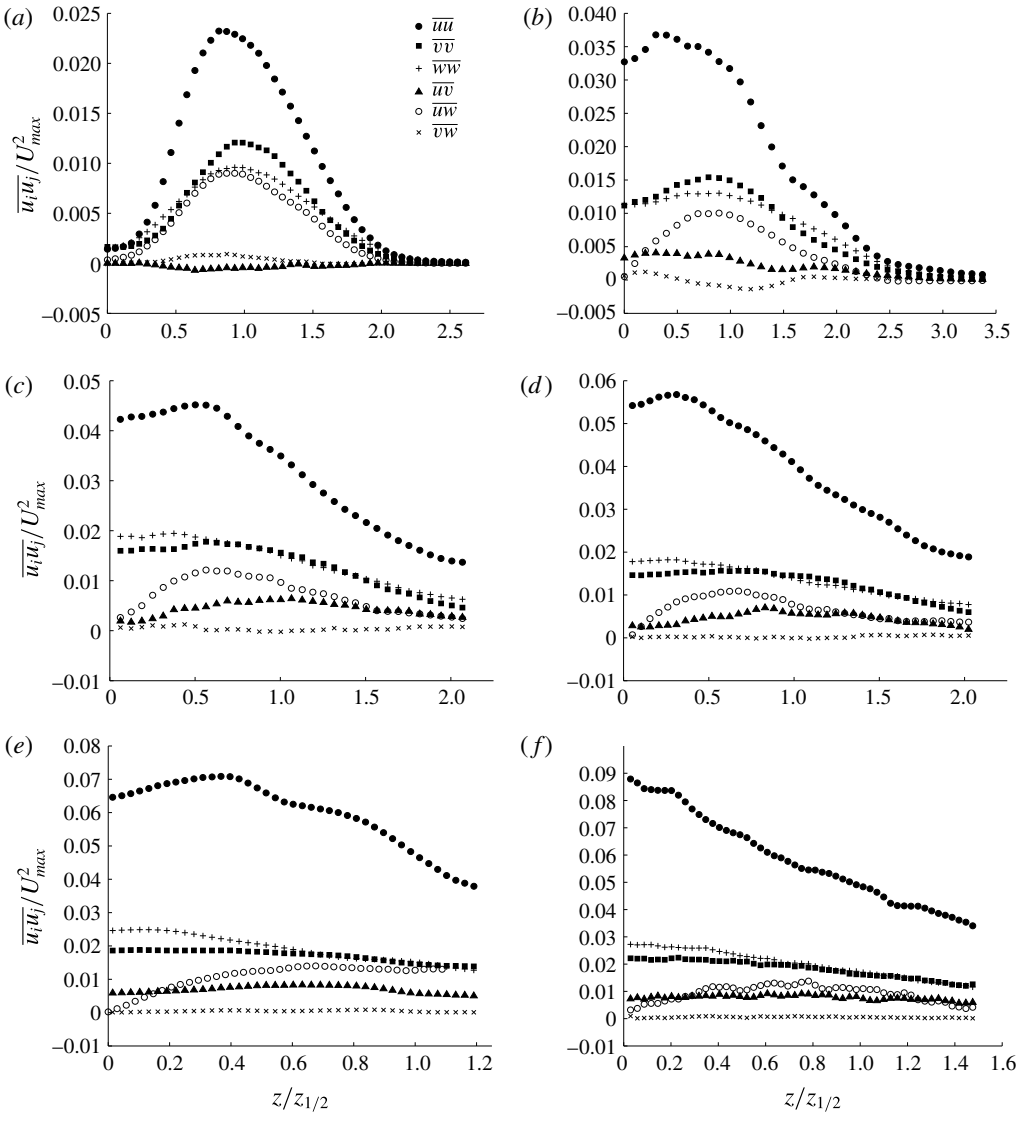

FIGURE 9. Profiles of the normalized Reynolds stresses measured across the jet at y_{max} for various streamwise locations: (*a*) $x/D = 5$, (*b*) $x/D = 10$, (*c*) $x/D = 15$, (*d*) $x/D = 20$, (*e*) $x/D = 30$ and (*f*) $x/D = 40$; (●) $\overline{uu}$, (■) $\overline{vv}$, (+) $\overline{ww}$, (▲) $\overline{uv}$, (○) $\overline{uw}$ and (×) $\overline{vw}$.

followed by $\overline{v^2}$ then $\overline{w^2}$. Unlike on the jet centreline, the $\overline{uw}$ shear stresses are now comparable to $\overline{w^2}$, whereas the magnitudes of $\overline{uv}$ and $\overline{vw}$ are small. By $x/D = 10$, the $\overline{w^2}$ values begin to become comparable to $\overline{v^2}$, and eventually overtake the $\overline{v^2}$ values at the middle of the jet at $x/D = 15$. This behaviour is probably due to the establishment of relatively larger lateral mean velocities in the jet at this point (Namgyal 2012). The values of $\overline{uv}$ are small and positive but are significantly larger than the $\overline{vw}$ shear stress across the jet.

The profiles of the Reynolds stresses point to a fairly complicated spatial variation in the Reynolds stresses. The physics of the flow and the relationship between the Reynolds stresses can be better understood by examining contours of the full flow

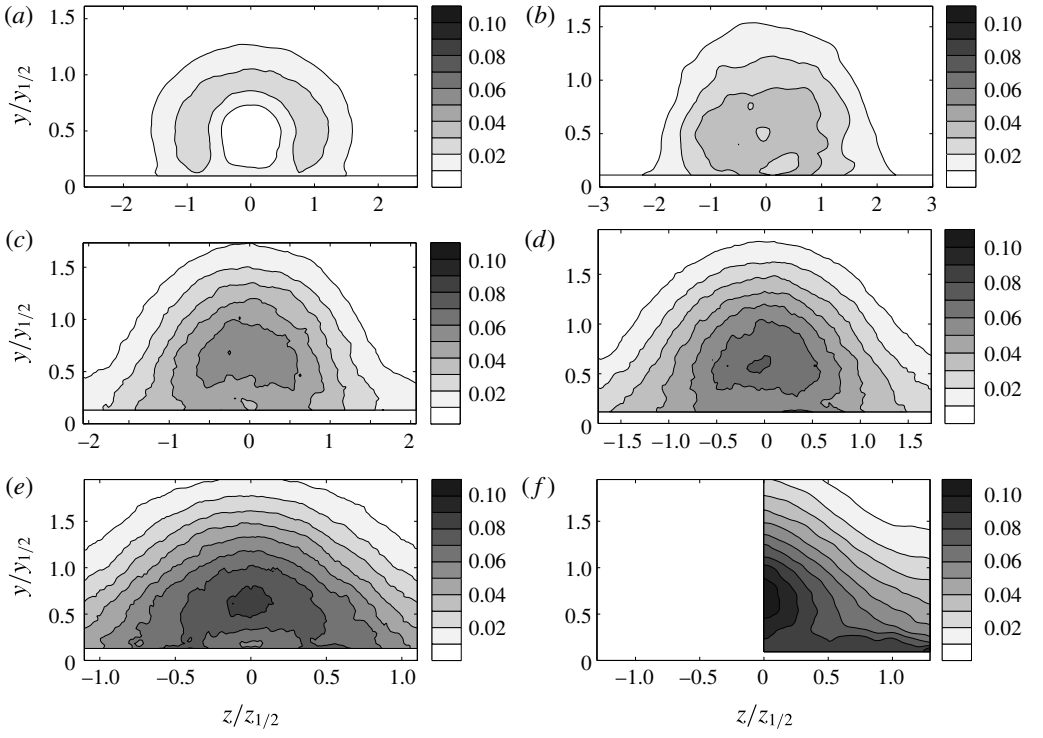

FIGURE 10. The normalized Reynolds normal stress, $\overline{u^2}/U_{max}^2$, at various downstream locations: (*a*) $x/D = 5$, (*b*) $x/D = 10$, (*c*) $x/D = 15$, (*d*) $x/D = 20$, (*e*) $x/D = 30$ and (*f*) $x/D = 40$.

field. Contours of the Reynolds stresses measured in the y–z plane are shown in figures 10–15. All of the stress contours are normalized by U_{max}^2 and the respective jet half-widths.

The normal stress contours at $x/D = 5$ have a prominent low-intensity circular region at the centre of the jet, indicating the existence of a potential core region at this location (i.e. figures 10*a*, 11*a* and 12*a*). As expected, the largest Reynolds normal stresses occur around the periphery of the jet in the outer shear layer, but by $x/D = 10$, the largest normal stresses tend to be located at the centre of the jet. The magnitudes of the normalized normal stresses are still increasing at $x/D = 40$, indicating that the flow is not self-similar by this point, consistent with the discussion of Craft & Launder (2001), who suggested that the turbulent three-dimensional wall jet may not truly become self-similar until $x/D > 100$.

The downstream evolution of the turbulent shear stresses, $\overline{uv}$, is shown in figure 13. Initially, there is a negative region near the wall and a positive region associated with the outer shear layer. Positive $\overline{uv}$ terms commonly occur in the free shear layers of jets and have been observed by several authors in the three-dimensional wall jet (Padmanabham & Gowda 1991*b*; Abrahamsson, Johansson & Lofdahl 1997*a*; Sun 2002). This outer positive region may be associated with the passage of a spanwise vorticity, $\overline{\Omega}_z$, which causes an event that drives the flow down and downstream (or up and upstream). The negative region is associated with the inner wall layer, consistent with the sign of $\overline{uv}$ observed in a boundary layer (Tachie 2000), near the wall in an impinging jet (Cooper *et al.* 1993) and in a plane wall jet (Eriksson *et al.*

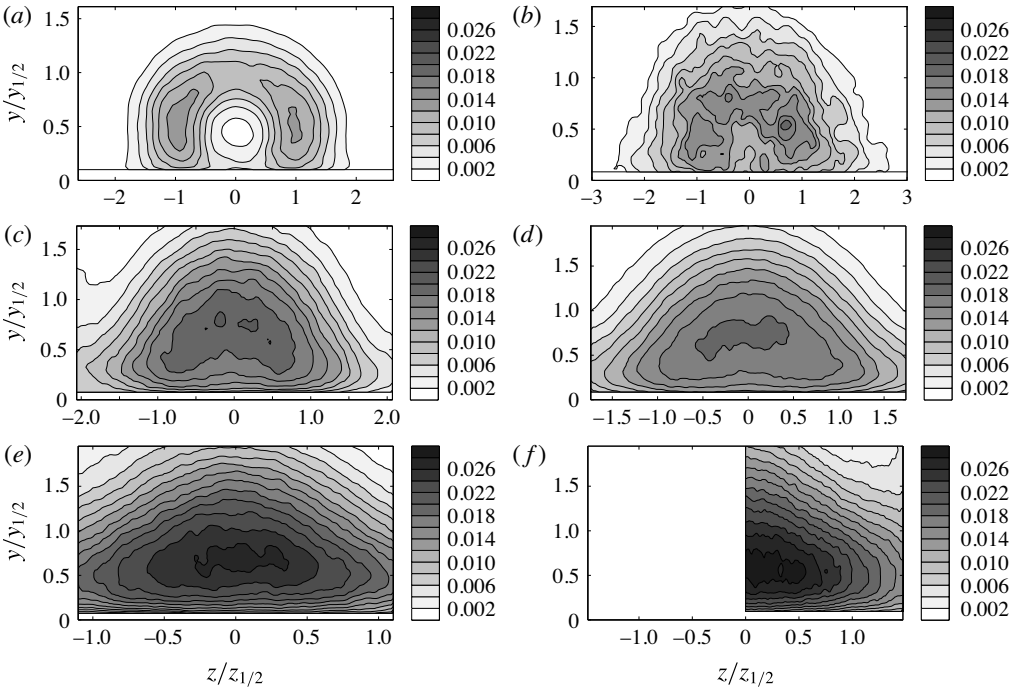

FIGURE 11. The normalized Reynolds normal stress, $\overline{v^2}/U_{max}^2$, at various downstream locations: (*a*) $x/D = 5$, (*b*) $x/D = 10$, (*c*) $x/D = 15$, (*d*) $x/D = 20$, (*e*) $x/D = 30$ and (*f*) $x/D = 40$.

1998; Rostamy *et al.* 2011). The negative near-wall region may be related to an event that causes a streamwise backflow and an ejection of fluid away from the wall, like the passage of a spanwise oriented vortex structure ($\overline{\Omega}_z$). As the flow evolves downstream, the outer positive region grows and suppresses the small negative region towards the jet centreline and down to the wall. This is consistent with the decrease of y_{max} noted at this point. By $x/D = 30$, there is no evidence of the negative region in the measurements; however, it is unclear whether this region has disappeared or has simply moved closer to the wall. Eriksson & Karlsson (2000) performed near-wall laser doppler anemometry measurements for the plane turbulent wall jet and showed that a large negative value of $\overline{uv}$ persists near the wall and has a local minima at $y^+ = 10$. Of course, we cannot resolve this close to the wall with our PIV measurements, so this suggests that there is probably an unresolved region of strong $\overline{uv}$ near the wall.

The contours of the turbulent shear stress, $\overline{uw}$, shown in figure 14, initially start out concentrated on either side of the jet centreline with opposite sign. These regions may be associated with a turbulent event that drives the flow into the streamwise direction and laterally outward, like a vertically oriented vortex ($\overline{\Omega}_y$) (consistent with coherent structure models in the jet (Namgyal 2012)). As the flow evolves downstream to $x/D = 10$ and then 15, these regions become wider, but by $x/D = 30$, they start to evolve downward towards the wall. This may be tied to the increasing large mean lateral velocities that persist near the wall in the jet.

The downstream variation of the $\overline{vw}$ contours is shown in figure 15. Initially, these regions are organized in four oppositely signed regions at $x/D = 5$. The reason for

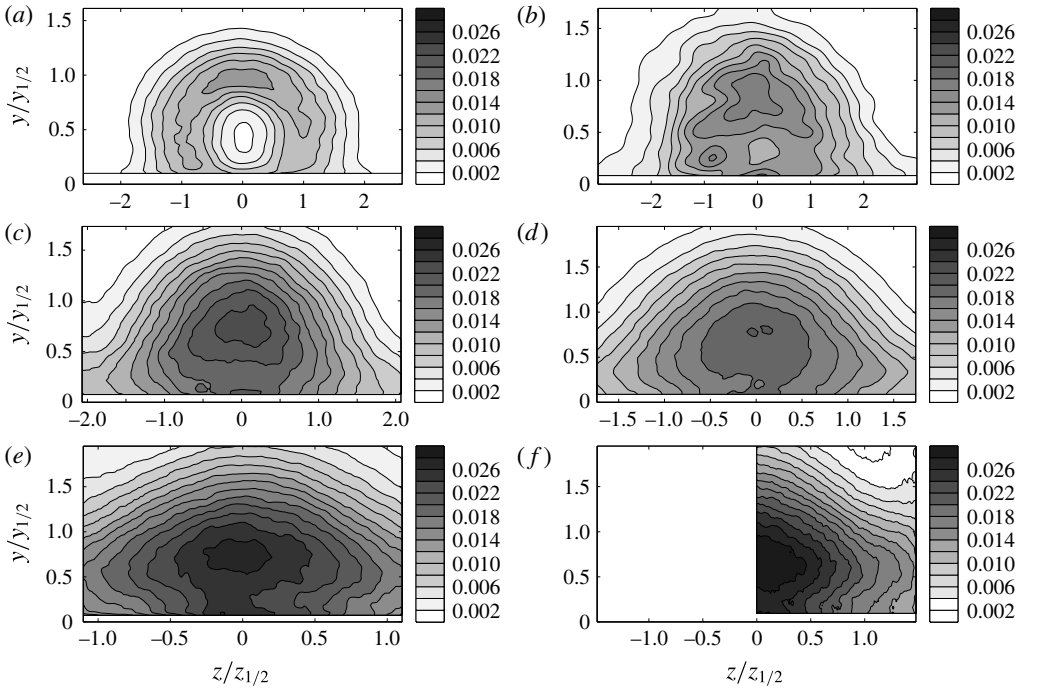

FIGURE 12. The normalized Reynolds normal stress, $\overline{w^2}/U_{max}^2$, at various downstream locations: (*a*) $x/D = 5$, (*b*) $x/D = 10$, (*c*) $x/D = 15$, (*d*) $x/D = 20$, (*e*) $x/D = 30$ and (*f*) $x/D = 40$.

this behaviour is unclear, although this term has been linked with the presence of streamwise vortices in free jets (Bradshaw 1987). As the flow evolves downstream, for example to $x/D = 15$ and 20, the upper two regions tend to diffuse outward and the lower two regions tend to get pushed down towards the wall. However, the relative magnitude of $\overline{vw}$ tends to decrease rapidly as the jet develops downstream. By $x/D = 30$ and 40, these regions become hard to distinguish due to the low magnitudes. These results suggests that $\overline{vw}$ plays only a minor role in the far-field development of the three-dimensional wall jet.

In order to understand the behaviour of the mean secondary flow in the three-dimensional turbulent wall jet, the distribution of the mean streamwise vorticity, $\overline{\Omega}_x$, is examined for various streamwise locations in figure 16. At $x/D = 5$, the contours of $\overline{\Omega}_x$ are dominated by a pair of oppositely signed regions located on either side of the jet centreline in the lateral shear layers (i.e. figure 16*a*). These regions correspond to the location of the near-wall bulging of the mean streamwise velocity contours, indicating that the streamwise vorticity is directly tied to the lateral growth of the flow, as expected. As the jet evolves further downstream, the outer regions of streamwise vorticity become more diffuse and begin to move away from the wall, consistent with the finding previously reported by Matsuda *et al.* (1990), Sun & Ewing (2002*b*) and Hall & Ewing (2007*a*). These regions are oriented to drive the flow down towards the wall and laterally outward. The inner regions of near-wall vorticity tend to spread outward along the wall, for example at $x/D = 20$ to 40; this behaviour has been attributed to the vortex tilting in the outer leg of the large-scale structures by Sun & Ewing (2002*b*).

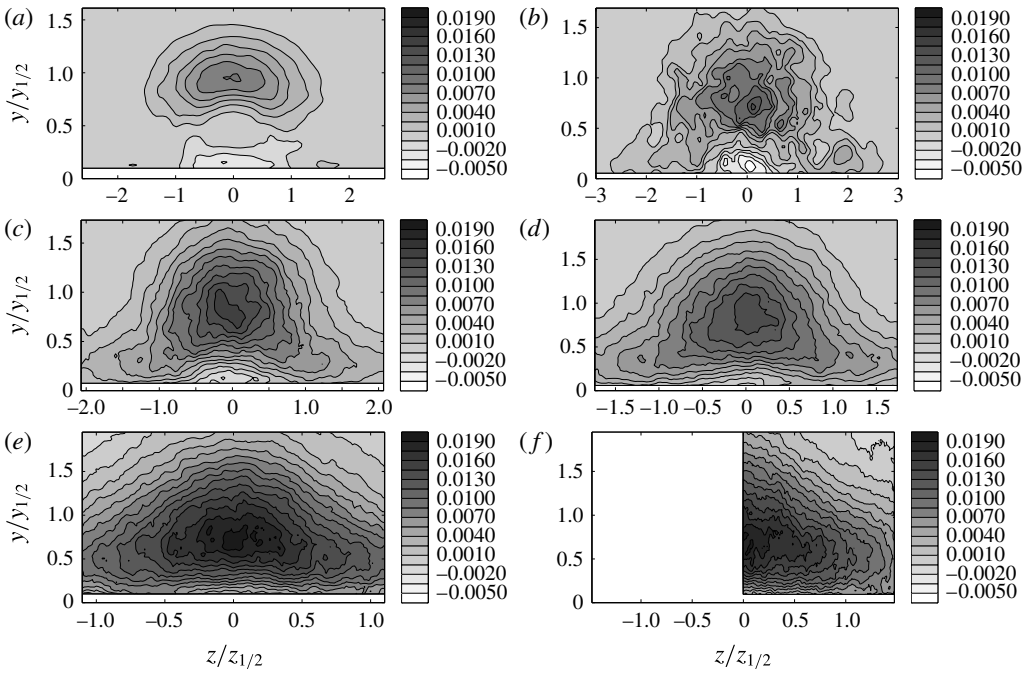

FIGURE 13. The normalized Reynolds shear stress, $\overline{uv}/U_{max}^2$, at various downstream locations: (*a*) $x/D = 5$, (*b*) $x/D = 10$, (*c*) $x/D = 15$, (*d*) $x/D = 20$, (*e*) $x/D = 30$ and (*f*) $x/D = 40$.

In order to improve our understanding of the sources of the turbulence generated secondary flow in the jet and the relative size of terms D and E in (1.1), profiles of the difference in the Reynolds normal stresses, $(\overline{v^2} - \overline{w^2})$ are compared with the Reynolds shear stress, $\overline{vw}$, on the jet centreline in figure 17. At $x/D = 5$ and 10, the profiles of $(\overline{v^2} - \overline{w^2})$ have two peaks located in the inner and outer shear-layer regions (figure 17*a*), and the contribution is significantly larger than $\overline{vw}$. The peak in $(\overline{v^2} - \overline{w^2})$ associated with the outer shear layers decreases, and by $x/D = 40$, $(\overline{v^2} - \overline{w^2})$ becomes negligible and comparable in magnitude to $\overline{vw}$ away from the wall. However, near the wall $(\overline{v^2} - \overline{w^2})$ continues to dominate at all downstream locations. It is apparent that the y gradient of $(\overline{v^2} - \overline{w^2})$ is much steeper near the wall.

A similar comparison is made for the Reynolds stresses, $(\overline{v^2} - \overline{w^2})$ and $\overline{vw}$, measured across one half of the jet at y_{max}, as shown in figure 18. Initially, the profiles of $(\overline{v^2} - \overline{w^2})$ have large peaks at $z/z_{1/2} = 1$ in the lateral shear layers. As the jet develops downstream to $x/D = 40$, this peak becomes negligible. Moreover, at all locations, $(\overline{v^2} - \overline{w^2})$ is significantly larger than $\overline{vw}$. Although the turbulence secondary flow is strictly tied to the spatial gradients of these terms, these results suggest that the difference in the normal stresses makes a much larger contribution than $\overline{vw}$.

Profiles of these two terms are useful to get a feel for the magnitude and trend associated with these terms, but a better representation of the size and total distribution of these terms can be gained by examining the contours of the full flow field. Contours of $(\overline{v^2} - \overline{w^2})$ and $\overline{vw}$ are shown in figure 19. For the purpose of comparing the relative magnitudes, both terms are plotted on the same contour level and are

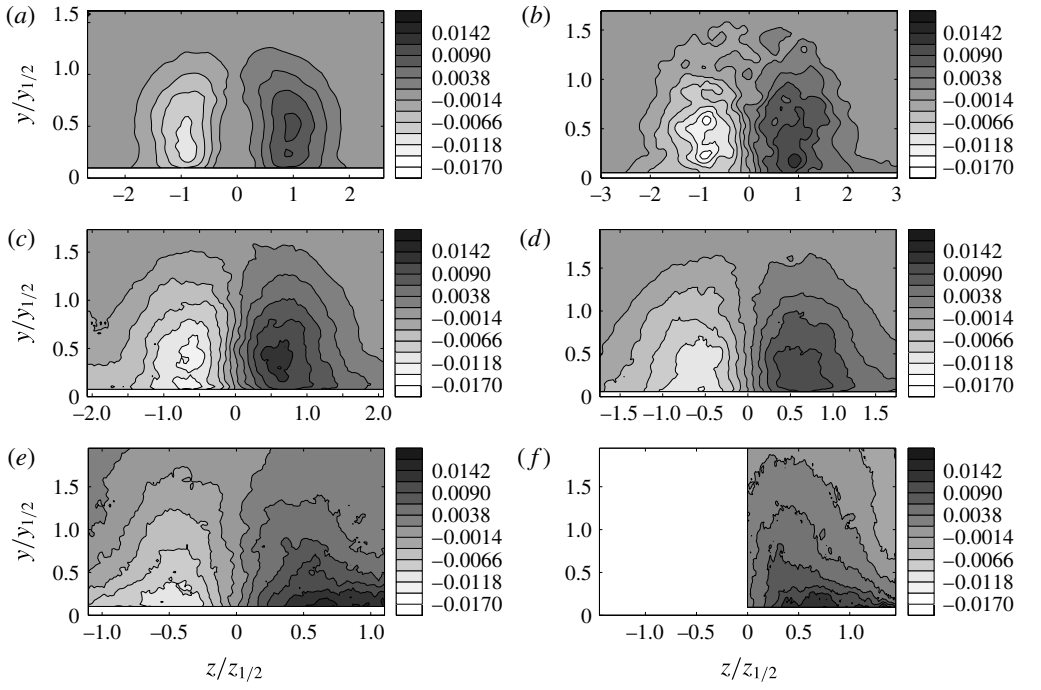

FIGURE 14. The normalized Reynolds shear stress, $\overline{uw}/U_{max}^2$, at various downstream locations: (*a*) $x/D = 5$, (*b*) $x/D = 10$, (*c*) $x/D = 15$, (*d*) $x/D = 20$, (*e*) $x/D = 30$ and (*f*) $x/D = 40$.

normalized by the square of the local maximum streamwise velocity, U_{max}^2. Initially, at $x/D = 5$, the contours of $(\overline{v^2} - \overline{w^2})$ have local maxima in the lateral shear layers and minima near the wall and in the outer shear layers. By $x/D = 15$, the large negative region of $(\overline{v^2} - \overline{w^2})$ spans the wall and persists as the jet evolves downstream, suggesting that its contribution does not decrease into the far field. At all downstream measurement locations, the contours indicate that the magnitude of $(\overline{v^2} - \overline{w^2})$ is much larger than that of $\overline{vw}$, particularly near the wall, although the magnitudes of $(\overline{v^2} - \overline{w^2})$ and $\overline{vw}$ are comparable away from the wall. This finding is also consistent with the findings of Brundrett & Baines (1964), who examined the turbulent generated mean secondary flows that persist in a square duct due to the corners, and with Xu (2009), who examined the mean secondary flows in a square annular duct flow. (It should be noted that the turbulent generated secondary flow in a square or rectangular duct causes a flow that is directed into the corners of a square duct. Unlike a square duct flow, the three-dimensional wall jet is unconfined, so the mean secondary flows influence the growth of the jet.) Both found that differences in the normal stresses were dominant near the wall. In fact, the relative magnitude of $\overline{vw}$ here seems to decrease as the jet evolves downstream, which suggests from a magnitude perspective only and not a gradient perspective that the relative importance of this term in the production of the turbulence generated secondary flow decreases into the far field. This again indicates that the differences in the cross-flow normal stresses are (from a magnitude perspective only) likely to be primarily responsible for the production of streamwise vorticity. The magnitude of the term is, by far, the highest near the wall.

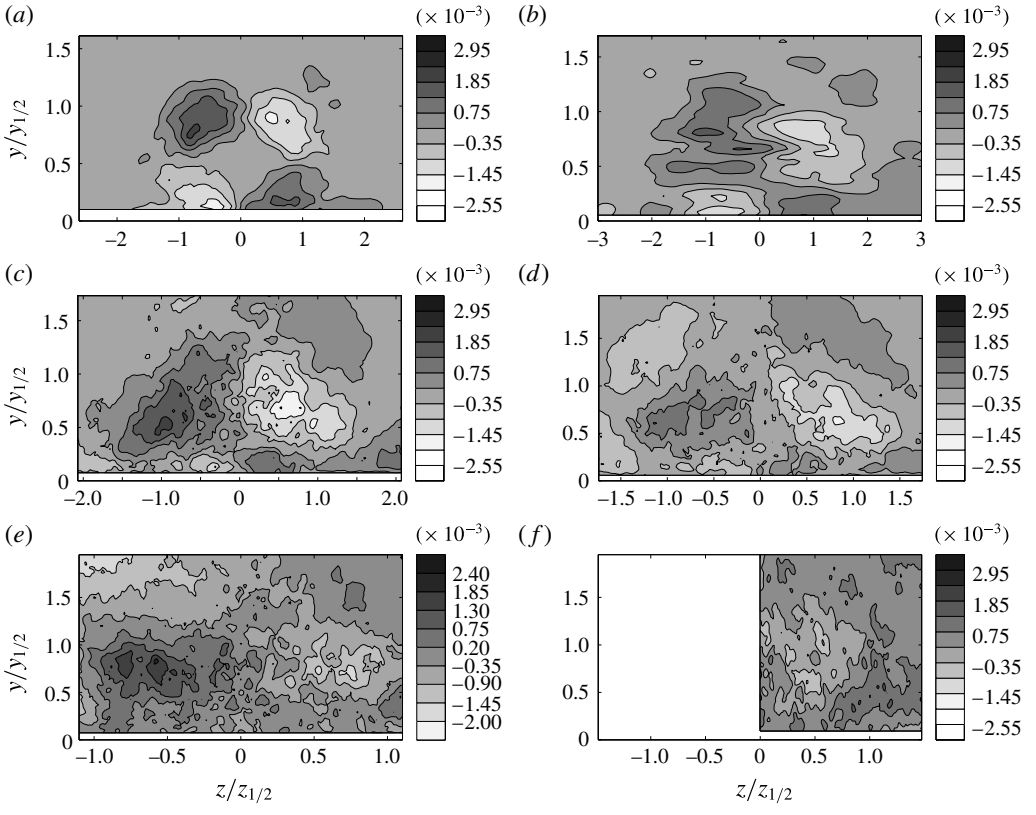

FIGURE 15. The normalized Reynolds shear stress, $\overline{vw}/U_{max}^2$, at various downstream locations: (*a*) $x/D = 5$, (*b*) $x/D = 10$, (*c*) $x/D = 15$, (*d*) $x/D = 20$, (*e*) $x/D = 30$ and (*f*) $x/D = 40$.

To truly quantify the actual sources of the turbulence generated secondary flow, information is required about the double spatial gradients of each of these terms. Every attempt was made at quantifying these sources, but as differentiation is a process that amplifies any noise in the measurements, the measurements were not resolved enough to yield satisfactory results. This is despite the fact that 3000 (near field) to 6000 (far field) statistically independent images were taken, many more than in any previous PIV study of the wall jet (Adane & Tachie 2010). Nevertheless, the measurements indicate that the difference in the cross-flow normal stresses is significantly larger than the cross-flow shear stress, and, thus, prior to taking the spatial derivatives term, D should make the largest contribution to the turbulence generated secondary flow.

The current results can also be used to determine whether the vorticity produced by the differences in the Reynolds normal stresses acts to reinforce or counteract the existing streamwise vorticity in the jet. Inspection of figure 19 (along with figures 17 and 18) reveals a rapid increase in the differences in the normal stresses in the y direction oriented to produce a positive gradient in the first quadrant. Similarly, inspection of the near-wall region of large negative $(\overline{v^2} - \overline{w^2})$ also reveals that the z gradient should be positive on the right side of the jet. Taken together, these results indicate that the differences in the Reynolds normal stresses near the wall

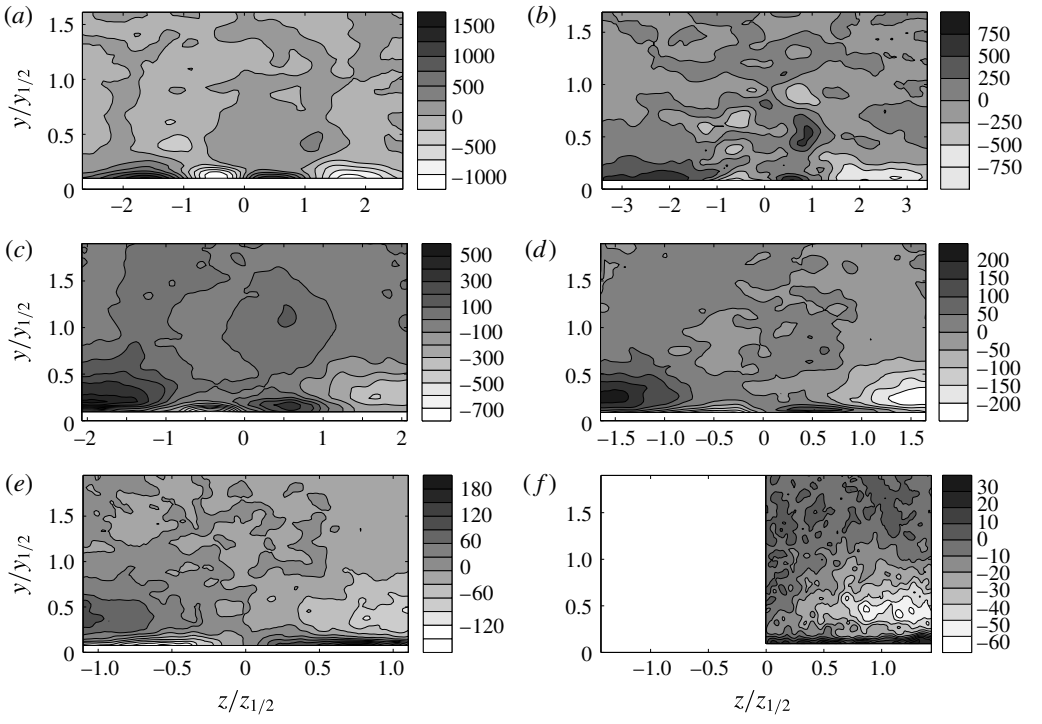

FIGURE 16. The mean streamwise vorticity, $\overline{\Omega}_x$ (1 s^{-1}), at various downstream locations: (*a*) $x/D = 5$, (*b*) $x/D = 10$, (*c*) $x/D = 15$, (*d*) $x/D = 20$, (*e*) $x/D = 30$ and (*f*) $x/D = 40$.

are oriented to produce positive streamwise vorticity on the right side of the jet. On the left side of the jet centreline, the z gradient is negative, so negative streamwise vorticity is then produced. Both of these sources are oriented to reinforce the mean near-wall streamwise vorticity in the jet, which, in turn, helps to sustain the large lateral development of this flow.

To help in understanding the underlying mechanism that sustains the turbulence, it is useful to examine the turbulent kinetic energy, $\overline{u_i u_i}$, and its associated distribution throughout the jet. The kinetic energy of the turbulent fluctuations for a Cartesian coordinate system is given by, for example, Mathieu & Scott (2000):

$$\underbrace{\frac{\partial \overline{q}}{\partial t}}_{\mathrm{I}} + \underbrace{\overline{U}_k \frac{\partial \overline{q}}{\partial x_k}}_{\mathrm{II}} = \underbrace{-\overline{u_i u_k}\frac{\partial \overline{U}_i}{\partial x_k}}_{\mathrm{III}} \underbrace{-\frac{\partial \overline{q u_k}}{\partial x_k}}_{\mathrm{IV}} \underbrace{-\frac{1}{\rho}\overline{u_i \frac{\partial p}{\partial x_i}}}_{\mathrm{V}} + \underbrace{\nu \overline{u_i \frac{\partial^2 u_i}{\partial x_k \partial x_k}}}_{\mathrm{VI}}, \tag{3.3}$$

where

$\overline{q} = (1/2)\overline{u_i u_i}$;

I – rate of increase of turbulent energy at a fixed point;

II – convection of turbulent energy by the mean flow;

III – production of turbulent energy by interaction between the mean flow and turbulence;

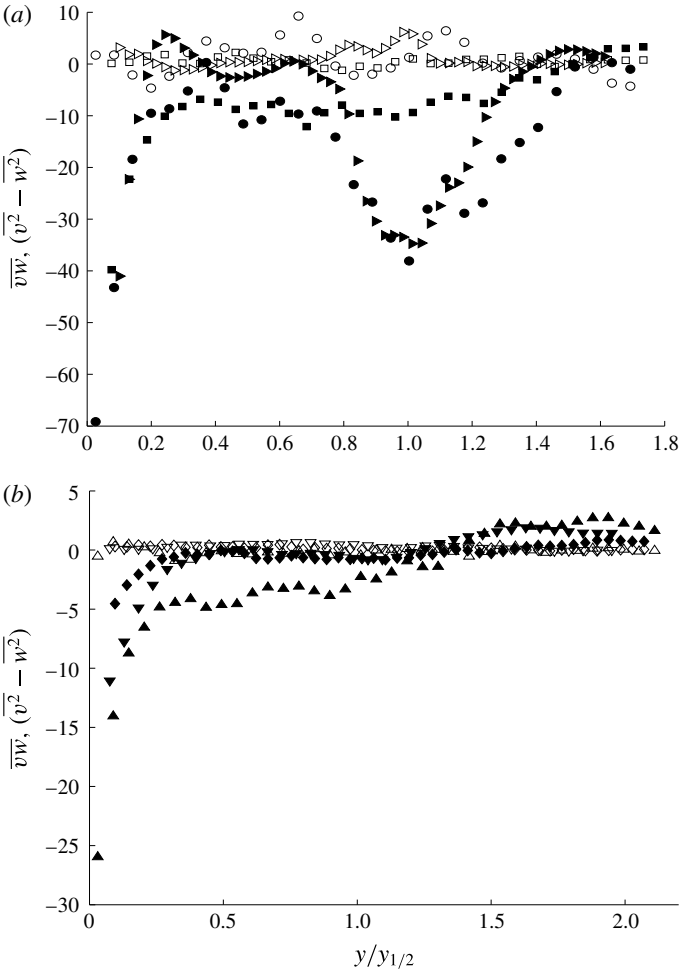

FIGURE 17. Profiles of the cross-flow Reynolds stresses, $(\overline{v^2} - \overline{w^2})$ and $\overline{vw}$ (m^2 s^{-2}), measured at the jet centreline for various streamwise locations: (*a*) $x/D = 5$ to 15 and (*b*) $x/D = 20$ to 40. The filled symbols represent $(\overline{v^2} - \overline{w^2})$ and the empty symbols represent $\overline{vw}$: (▶) and (▷) $x/D = 5$, (●) and (○) $x/D = 10$, (■) and (□) $x/D = 15$, (△) and (▲) $x/D = 20$, (▽) and (▼) $x/D = 30$, and (◇) and (◆) $x/D = 40$.

IV – convective transport of turbulent energy by the fluctuating motion (turbulent mixing);

V – transfer of turbulent energy by pressure effects;

VI – viscous effects (dissipation, diffusion).

Determination of the kinetic energy budget in the three-dimensional wall jet has only received limited attention in the literature. For example, Abrahamsson *et al.* (1997*a*) measured all three components of the kinetic energy and four of nine turbulent production terms at the jet centreline for the three-dimensional wall jet at $x/D = 80$. Padmanabham & Gowda (1991*b*) measured three turbulent production terms for the wall jet, again at the jet centreline, for the inlet nozzle configuration

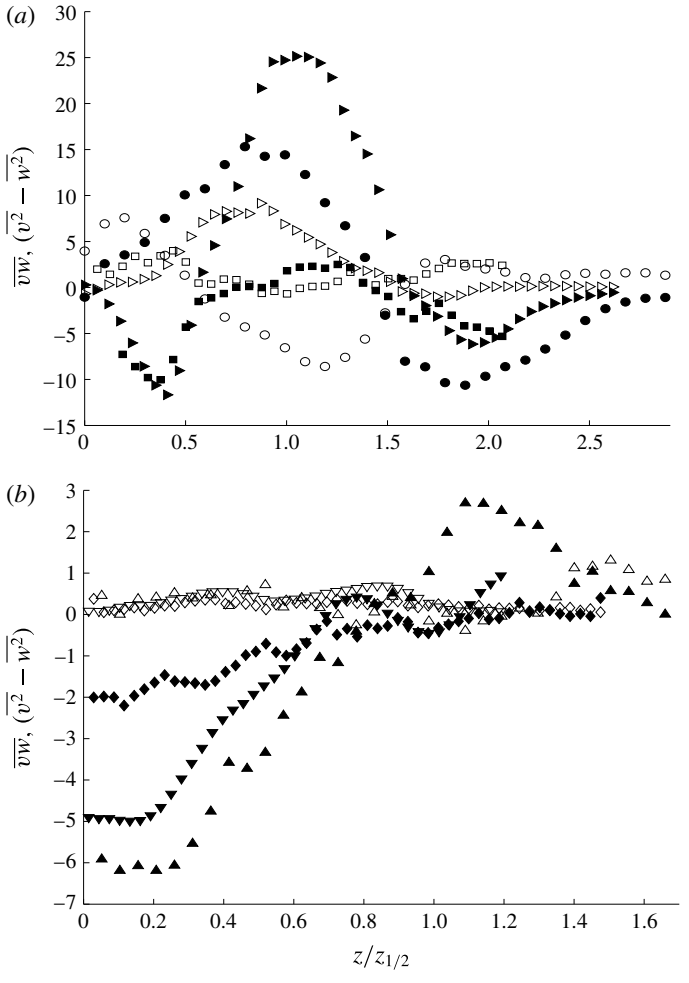

FIGURE 18. Profiles of the cross-flow Reynolds stresses, $(\overline{v^2} - \overline{w^2})$ and $\overline{vw}$ (m^2 s^{-2}), measured parallel across the wall at y_{max}: (*a*) $x/D = 5$ to 15 and (*b*) $x/D = 20$ to 40. The filled symbols represent $(\overline{v^2} - \overline{w^2})$ and the empty symbols represent $\overline{vw}$: (▶) and (▷) $x/D = 5$, (●) and (○) $x/D = 10$, (■) and (□) $x/D = 15$, (△) and (▲) $x/D = 20$, (▽) and (▼) $x/D = 30$, and (◇) and (◆) $x/D = 40$.

$h/D = 0.8$ at $x/D = 60$. However, until now, there is no information about the kinetic energy and production terms off the centreline of the jet. Having this information off the centreline is crucial to improving our understanding of this flow, as a number of the Reynolds stresses are the largest away from the jet centreline.

In order to better understand the turbulent mechanisms that sustain the flow, the production of turbulent kinetic energy by the interaction of mean flow and turbulence, $-\overline{u_i u_k}(\partial \overline{U_i}/\partial x_k)$, is examined. Expanding the term $-\overline{u_i u_k}(\partial \overline{U_i}/\partial x_k)$ yields

$$-\overline{u_i u_k}\frac{\partial \overline{U_i}}{\partial x_k} = -\overline{uu}\frac{\partial \overline{U}}{\partial x} - \overline{uv}\frac{\partial \overline{U}}{\partial y} - \overline{uw}\frac{\partial \overline{U}}{\partial z} - \overline{uv}\frac{\partial \overline{V}}{\partial x} - \overline{vv}\frac{\partial \overline{V}}{\partial y} - \overline{vw}\frac{\partial \overline{V}}{\partial z} - \overline{uw}\frac{\partial \overline{W}}{\partial x} - \overline{vw}\frac{\partial \overline{W}}{\partial y} - \overline{ww}\frac{\partial \overline{W}}{\partial z}. \tag{3.4}$$

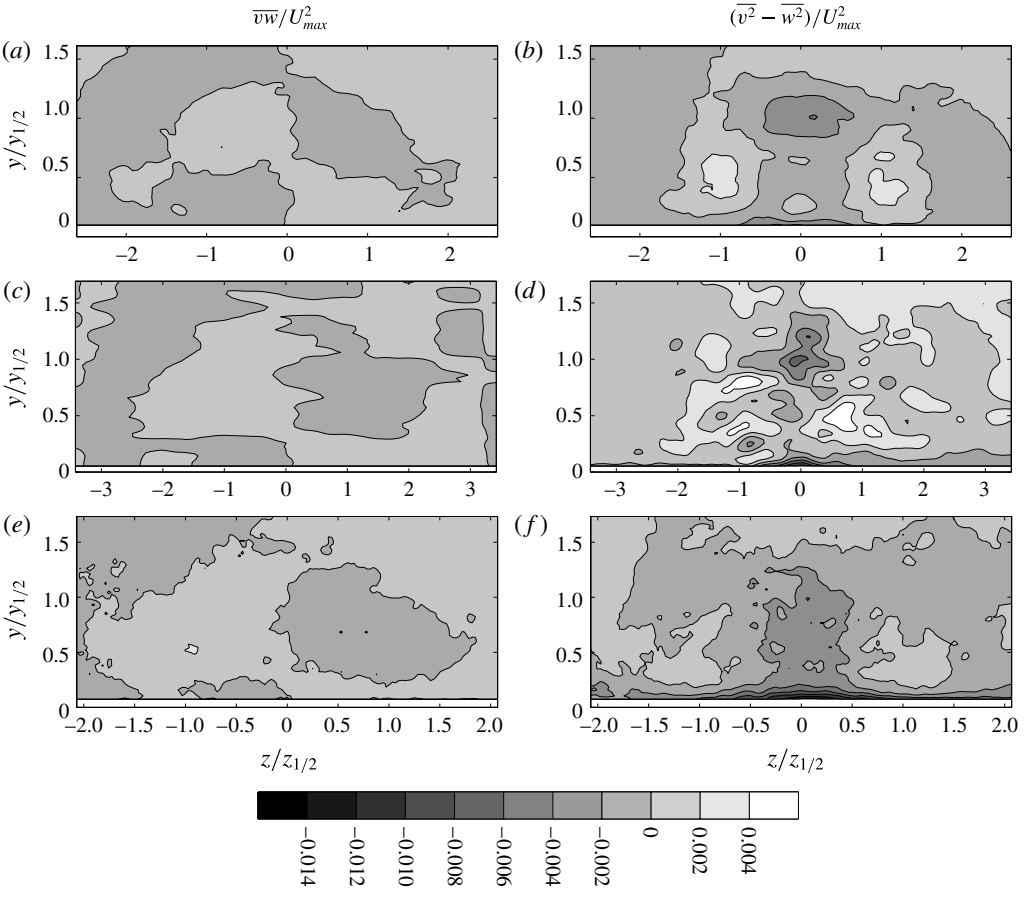

FIGURE 19. For caption see next page.

Of the nine production terms, only the six production terms that are associated with the spatial derivatives with respect to y and z can be computed here as there is no information about the streamwise spatial gradients. However, in the intermediate field and on towards the far field it is likely that the jet only changes slowly in the x direction, and thus the contribution from these terms will be assumed to be negligible. This assumption was also used by Wygnanski & Fiedler (1969) in their study of the turbulent kinetic energy budget of a turbulent free jet. However, some care should be taken in interpreting these terms in the three-dimensional wall jet, as Abrahamsson *et al.* (1997*a*) have shown that $-\overline{uu}(\partial\overline{U}/\partial x)$ makes a significant contribution to the production close to the wall on the jet centreline.

Contours of each of the production terms are compared at $x/D=5$, 20 and 30 in figures 20–22. These contours are compared with the turbulent kinetic energy, q, and the sum of all of the production terms that could be measured here:

$$P=-\overline{uv}\frac{\partial\overline{U}}{\partial y}-\overline{uw}\frac{\partial\overline{U}}{\partial z}-\overline{vv}\frac{\partial\overline{V}}{\partial y}-\overline{vw}\frac{\partial\overline{V}}{\partial z}-\overline{vw}\frac{\partial\overline{W}}{\partial y}-\overline{ww}\frac{\partial\overline{W}}{\partial z}. \tag{3.5}$$

In the near field at $x/D=5$, by far the largest contributions to the production come from the shear stress terms $-\overline{uv}(\partial\overline{U}/\partial y)$ and $-\overline{uw}(\partial\overline{U}/\partial z)$, with the contribution from

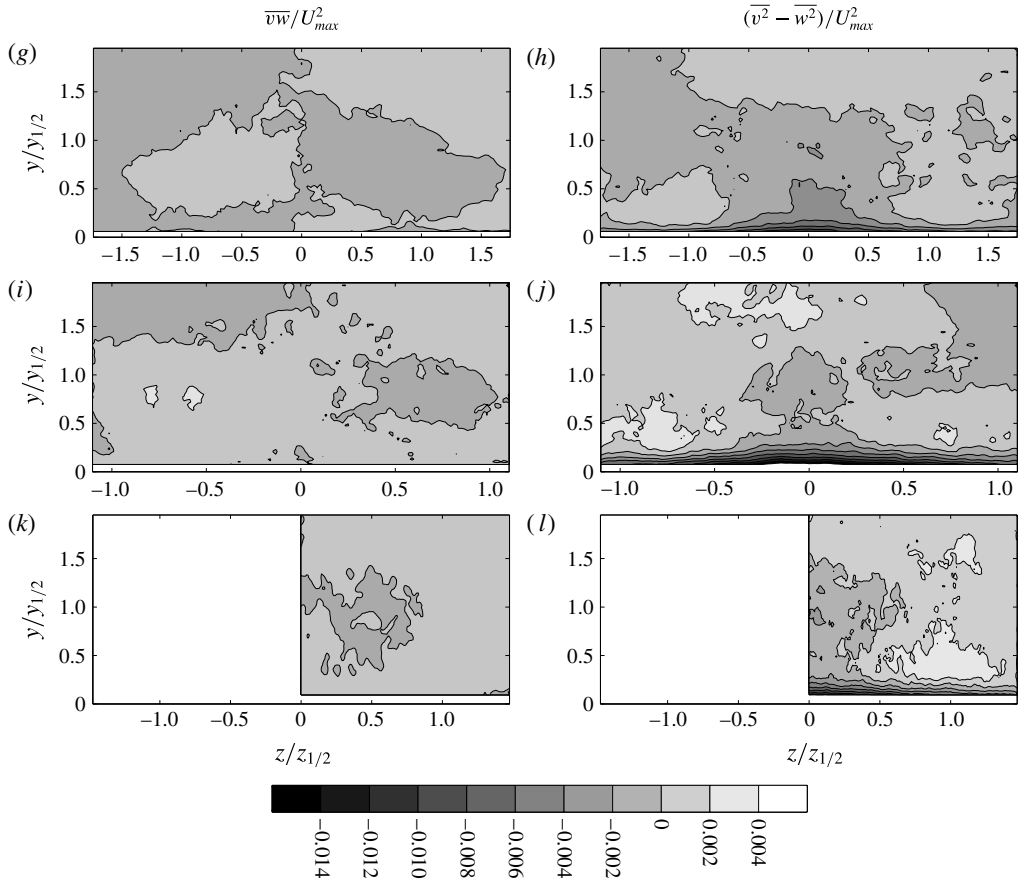

FIGURE 19. (cntd). Comparison of the normalized cross-flow Reynolds stresses, $\overline{vw}//U_{max}^2$ and $(\overline{v^2}-\overline{w^2})/U_{max}^2$, at various streamwise locations: (*a*,*b*) $x/D=5$, (*c*,*d*) $x/D=10$, (*e*,*f*) $x/D=15$, (*g*,*h*) $x/D=20$, (*i*,*j*) $x/D=30$ and (*k*,*l*) $x/D=40$.

each of the terms being similar in magnitude and being roughly an order of magnitude larger than all of the other production terms. The $-\overline{uv}(\partial\overline{U}/\partial y)$ production term is largest in the upper shear layer of the jet, principally due to the large values of $\overline{uv}$ here and the large mean streamwise velocity, although there is a relatively strong region of production near the wall associated with this term at the jet centreline. Similarly, the large streamwise flow velocity and the large value of $\overline{uw}$ associated with the lateral shear layers also cause the $-\overline{uw}(\partial\overline{U}/\partial z)$ term to be large. All of the other production terms are much smaller and occur in much smaller localized regions. When all of the contributions to the production are summed, the contours of P indicate that the turbulent kinetic energy is produced in the shear layers of the jet. The contours of turbulent kinetic energy look very much like the production contours at this position.

Further downstream, at $x/D=20$, it is apparent that the shear stress terms $-\overline{uv}(\partial\overline{U}/\partial y)$ and $-\overline{uw}(\partial\overline{U}/\partial z)$ still make the largest contributions to the turbulent production; however, the term $-\overline{uv}(\partial\overline{U}/\partial y)$ is making a proportionally larger contribution. The contours associated with $-\overline{uv}(\partial\overline{U}/\partial y)$ are still the largest near the centre of the jet and are spreading upwards and laterally, but are still probably associated with the turbulence in the upper shear layer. The contours associated with

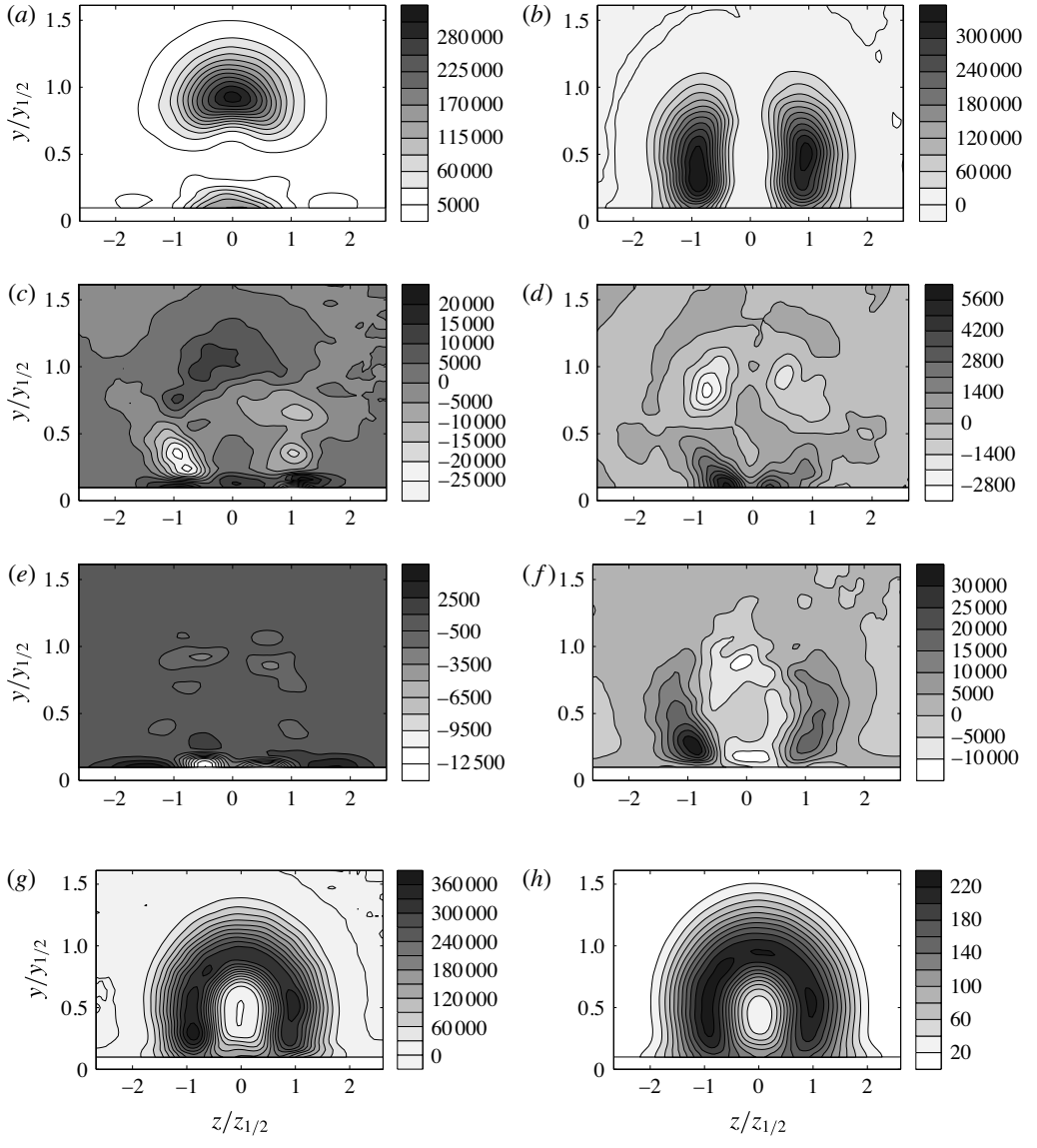

FIGURE 20. Contours of turbulent kinetic energy ($m^2\ s^{-2}$) and turbulent production terms ($m^2\ s^{-3}$) at $x/D = 5$: (*a*) $-\overline{uv}(\partial\overline{U}/\partial y)$, (*b*) $-\overline{uw}(\partial\overline{U}/\partial z)$, (*c*) $-\overline{vv}(\partial\overline{V}/\partial y)$, (*d*) $-\overline{vw}(\partial\overline{V}/\partial z)$, (*e*) $-\overline{vw}(\partial\overline{W}/\partial y)$, (*f*) $-\overline{ww}(\partial\overline{W}/\partial z)$, (*g*) P and (*h*) $\overline{q}$.

$-\overline{uw}(\partial\overline{U}/\partial z)$ are still large, but are smaller primarily because the large lateral width of the jet is causing $\partial\overline{U}/\partial z$ to become smaller. The other production terms are again much smaller. The contours of P are much more diffuse than at $x/D = 5$ and are primarily associated with the nominal position of the outer shear layers in the jet. The P contours still do loosely resemble the contours of turbulent kinetic energy, but the turbulent kinetic energy is the highest in the centre of the jet and down towards the wall. It should be noted that near the wall at the jet centreline the turbulent kinetic energy is large and there is low production at this point; this could be due to the transport or diffusion or to a production term that we cannot measure.

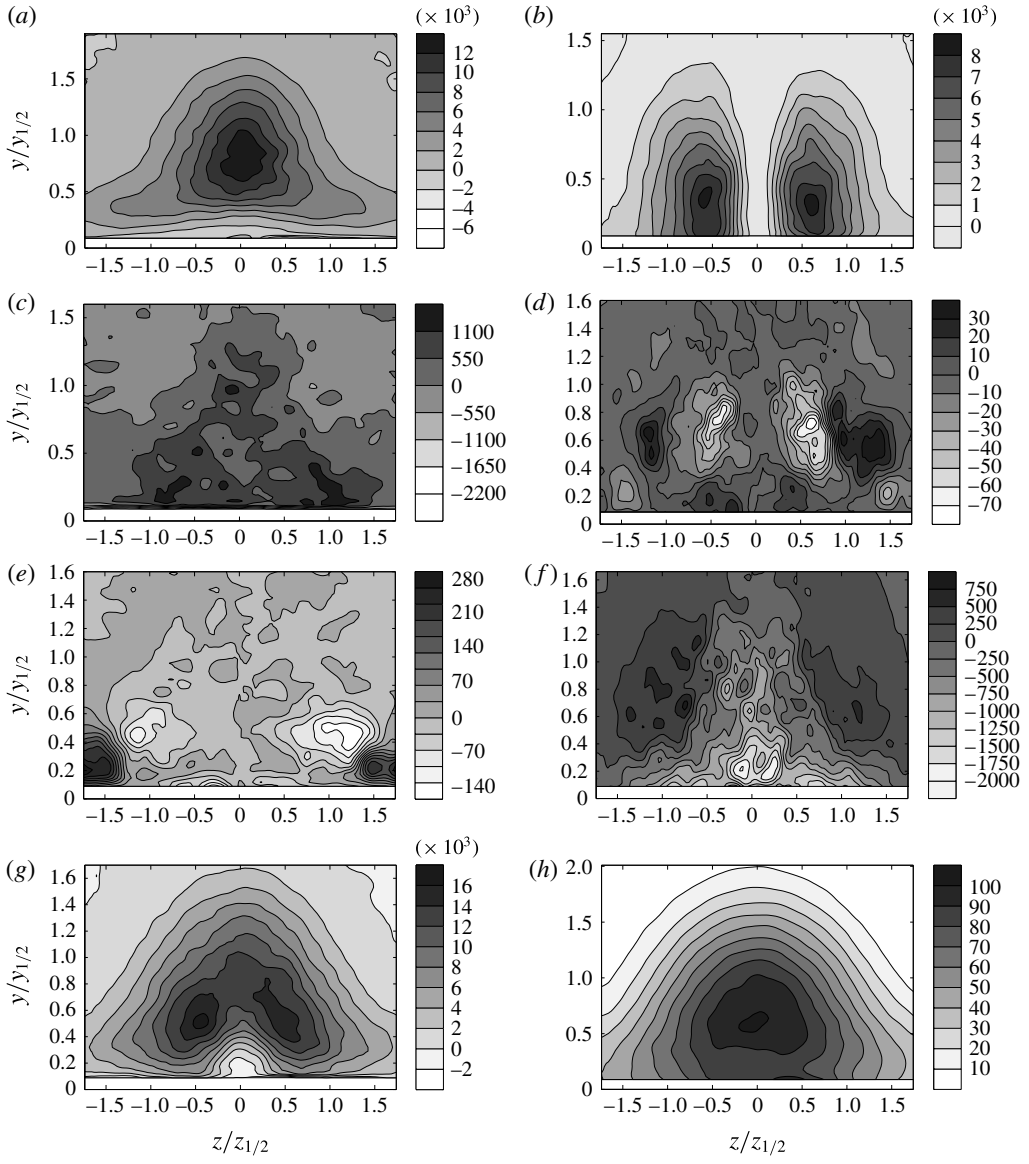

FIGURE 21. Contours of turbulent kinetic energy ($m^2\ s^{-2}$) and turbulent production terms ($m^2\ s^{-3}$) at $x/D = 20$: (*a*) $-\overline{uv}(\partial\overline{U}/\partial y)$, (*b*) $-\overline{uw}(\partial\overline{U}/\partial z)$, (*c*) $-\overline{vv}(\partial\overline{V}/\partial y)$, (*d*) $-\overline{vw}(\partial\overline{V}/\partial z)$, (*e*) $-\overline{vw}(\partial\overline{W}/\partial y)$, (*f*) $-\overline{ww}(\partial\overline{W}/\partial z)$, (*g*) P and (*h*) $\overline{q}$.

At $x/D = 30$, although the contributions from $-\overline{uv}(\partial\overline{U}/\partial y)$, and $-\overline{uw}(\partial\overline{U}/\partial z)$ are still dominant, the contribution from $-\overline{uw}(\partial\overline{U}/\partial z)$ continues to decrease and is now approximately half the size of $-\overline{uv}(\partial\overline{U}/\partial y)$. The contours of $-\overline{uv}(\partial\overline{U}/\partial y)$ are much larger and broader with the largest values occurring in the outer shear layers at the jet centreline. The contours of $-\overline{uw}(\partial\overline{U}/\partial z)$ are tending down towards the wall and are getting much more localized, consistent with the downward trend for $\overline{uw}$ with increasing downstream distance shown earlier. The contours of $-\overline{uw}(\partial\overline{U}/\partial z)$ for $x/D = 40$, not shown here for the sake of brevity, indicate that the largest region of production gets still closer to the wall and the magnitude gets smaller with respect

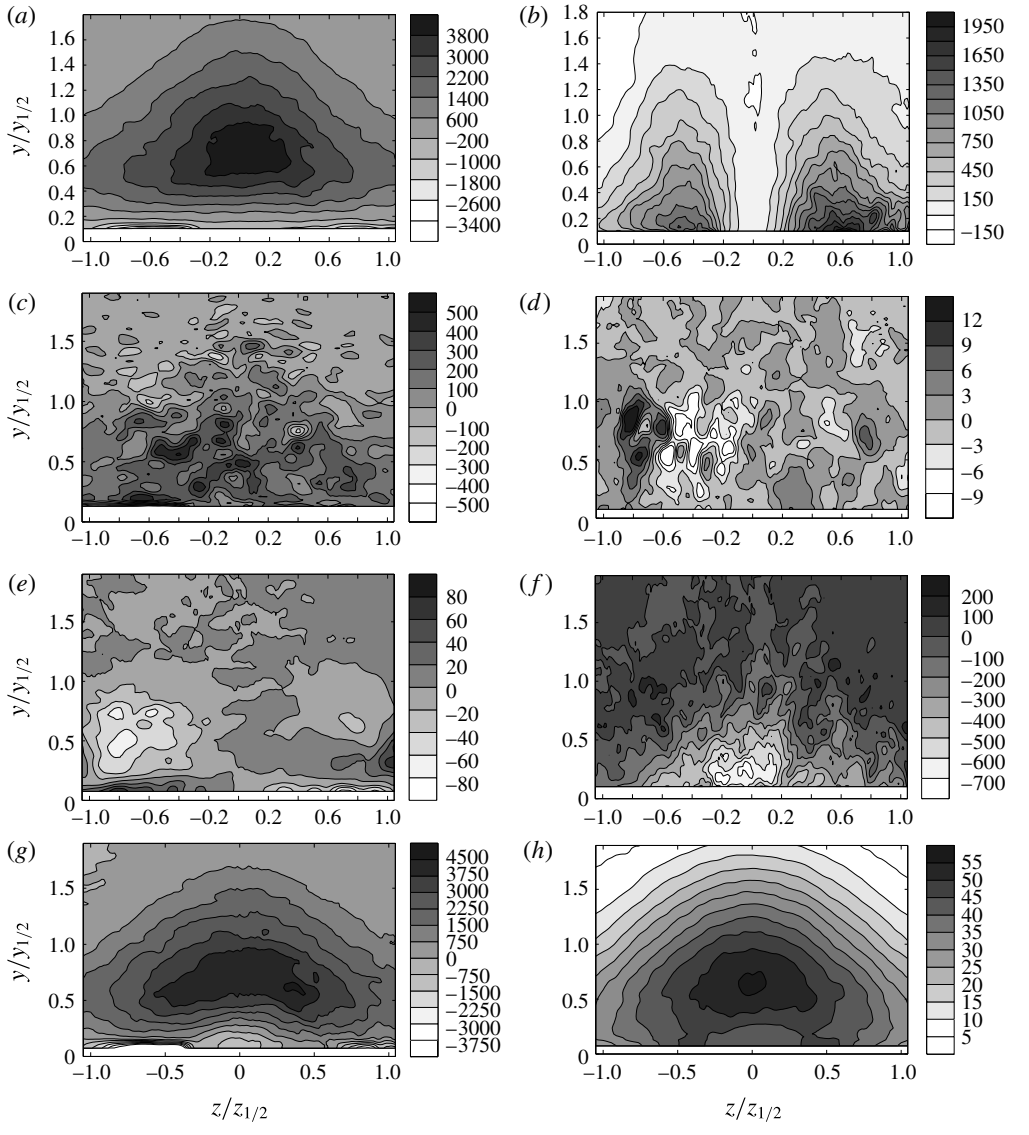

FIGURE 22. Contours of turbulent kinetic energy ($m^2\ s^{-2}$) and turbulent production terms ($m^2\ s^{-3}$) at $x/D = 30$: (*a*) $-\overline{uv}(\partial\overline{U}/\partial y)$, (*b*) $-\overline{uw}(\partial\overline{U}/\partial z)$, (*c*) $-\overline{vv}(\partial\overline{V}/\partial y)$, (*d*) $-\overline{vw}(\partial\overline{V}/\partial z)$, (*e*) $-\overline{vw}(\partial\overline{W}/\partial y)$, (*f*) $-\overline{ww}(\partial\overline{W}/\partial z)$, (*g*) P and (*h*) $\overline{q}$.

to $-\overline{uv}(\partial\overline{U}/\partial y)$. The contours of total production, P, strongly resemble the term $-\overline{uv}(\partial\overline{U}/\partial y)$, and both strongly resemble the contours of turbulent kinetic energy. It should be noted that even though the contours of $-\overline{uw}(\partial\overline{U}/\partial z)$ are large near the wall, they seem to be negated by the negative near-wall contributions by $-\overline{ww}(\partial\overline{W}/\partial z)$, so that the near-wall contribution is negligible in P.

It is unexpected that, in a flow with such strong lateral velocities and large lateral growth, the contribution of the lateral shear stresses plays a diminishing role in the production of turbulence as the jet evolves into the far field. It has been suggested by Craft & Launder (2001) that the large lateral growth of the three-dimensional wall

jet indicates that the jet is not yet fully developed and that it may not reach the far field until 100 diameters downstream. Perhaps this change in the turbulent production mechanism is also related to the slow development of this flow.

The convection of turbulent kinetic energy by the turbulent motions (the mixing term IV in (3.3)) is also examined. This term can be expanded to yield

$$\begin{aligned} -\frac{\partial \overline{qu_k}}{\partial x_k} &= -\frac{\partial}{\partial x_k}\left(\frac{1}{2}\overline{u_i u_i u_k}\right) \\ &= -\frac{\partial}{\partial x}\left(\frac{1}{2}\overline{u^2 u}\right) - \frac{\partial}{\partial y}\left(\frac{1}{2}\overline{u^2 v}\right) - \frac{\partial}{\partial z}\left(\frac{1}{2}\overline{u^2 w}\right) - \frac{\partial}{\partial x}\left(\frac{1}{2}\overline{v^2 u}\right) \\ &\quad - \frac{\partial}{\partial y}\left(\frac{1}{2}\overline{v^2 v}\right) - \frac{\partial}{\partial z}\left(\frac{1}{2}\overline{v^2 w}\right) - \frac{\partial}{\partial x}\left(\frac{1}{2}\overline{w^2 u}\right) - \frac{\partial}{\partial y}\left(\frac{1}{2}\overline{w^2 v}\right) \\ &\quad - \frac{\partial}{\partial z}\left(\frac{1}{2}\overline{w^2 w}\right). \end{aligned} \tag{3.6}$$

Again, x derivatives could not be computed here, but as the jet develops slowly in the intermediate and far field, although not shown here, the results indicate that the second and third terms make the largest contributions to the mixing term. Contours of the turbulent mixing term at $x/D = 5$, 20 and 30 are included in the Appendix for comparison.

The convection of turbulent kinetic energy by the mean flow, term II in (3.3), is also examined. When expanded, the full convection term is represented by

$$\overline{U_k}\frac{\partial \overline{q}}{\partial x_k} = \overline{U}\frac{\partial \overline{q}}{\partial x} + \overline{V}\frac{\partial \overline{q}}{\partial y} + \overline{W}\frac{\partial \overline{q}}{\partial z}. \tag{3.7}$$

The first term could not be computed here as there is no information about the streamwise variation of $\overline{q}$, and the total convection of turbulent kinetic energy by the mean flow is approximated by the second two terms. It should be noted that this approximation is probably not as good as for the earlier mixing or production terms, as even though $\partial\overline{q}/\partial x$ can be expected to be small in the intermediate and far field, $\overline{U}$ is by far the largest mean velocity component. Nevertheless, some insight into the turbulent kinetic energy can be gained by examining these contours. Contours of the turbulent mixing term at $x/D = 5$, 20 and 30 are also included in the Appendix for comparison.

The production, mixing and convection of turbulent kinetic energy are plotted on the same contour levels and compared at $x/D = 5$, 20 and 30 in figures 23–25 to allow for an examination of the turbulent energy budget in the three-dimensional wall jet. Here, contours of the turbulent kinetic energy, $\overline{q}$, are also included for the purpose of comparison.

At $x/D = 5$, the production is largest in the shear layer and makes by far the largest contribution to the turbulent energy budget. This production is balanced by the turbulent transport of energy out of the shear-layer region, and a corresponding increase in turbulent transport in the potential core region and outside of the shear layers (particularly in the lateral shear layers). (More information can be gained by examining this term and the mean term plotted on different contours levels in figure 26 in the Appendix.) The convection of turbulent kinetic energy by the mean (the in-plane term) is quite small but is positive inside the shear layers and negative outside of the shear layers.

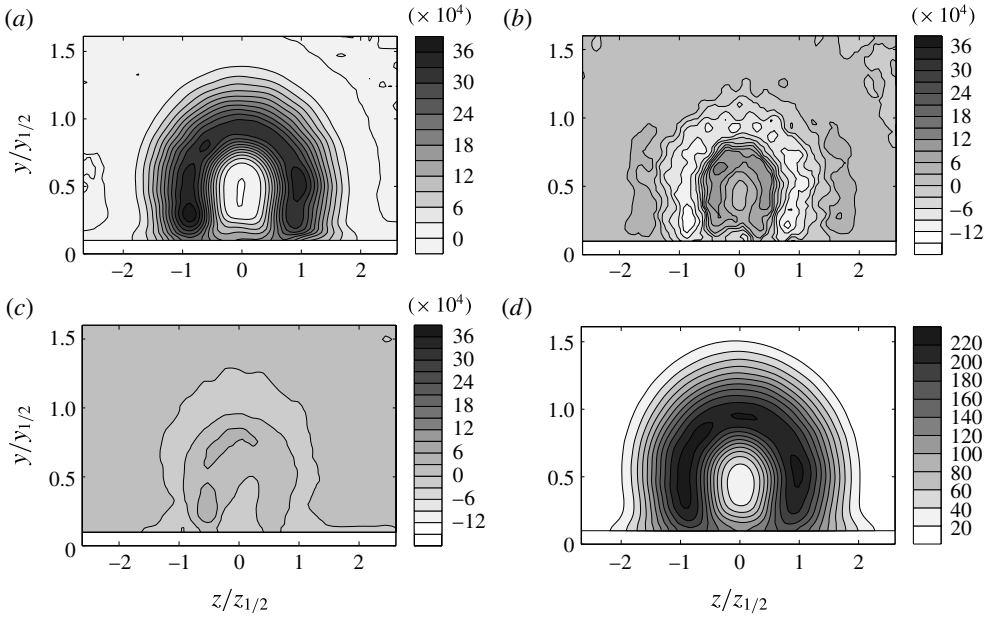

FIGURE 23. Contours of the turbulent kinetic energy budget at $x/D = 5$: (*a*) turbulent production, P (m^2 s^{-3}), (*b*) convection of turbulent energy by turbulence, $-((\partial\overline{qv}/\partial y) + (\partial\overline{qw}/\partial z))$ (m^2 s^{-3}), (*c*) convection of turbulent energy by mean, $(\overline{V}(\partial\overline{q}/\partial y) + \overline{W}(\partial\overline{q}/\partial z))$ (m^2 s^{-3}), and (*d*) turbulent kinetic energy, $(\overline{q})$ (m^2 s^{-2}).

Further downstream at $x/D = 20$, as shown in figure 24, the production again makes the largest contribution to the turbulent kinetic energy budget and resembles the contours of turbulent kinetic energy except near the wall at the jet centreline. This region corresponds to a large positive region of turbulent diffusion. Again, there is a large region of negative turbulent diffusion where the production is the highest, and this is offset by positive diffusion outside of the outer shear layers and the aforementioned large positive region. This near-wall region of positive turbulent diffusion at the centreline is also apparent at $x/D = 30$ and again offsets the region of low production in this area. At both $x/D = 20$ and 30 the mean convective term is again quite small in relation to the other terms but indicates that there is a negative region that persists near the wall and is probably tied to the large lateral velocities in the jet at this location. Most importantly, it should be noted that examining the terms in the turbulent energy budget along the jet centreline only would give a very different turbulent energy budget than on either side of the jet centreline.

4. Concluding remarks

Three-component velocity measurements were performed in the cross-flow plane of the turbulent three-dimensional wall jet. The results indicate that on average, the jet entrains air down towards the wall and ejects it laterally outward. The measurements were of sufficient resolution so that mass and momentum flux could be computed for the first time in the three-dimensional wall jet. The mass flux measurements indicate that the entrainment of ambient fluid increases linearly in the wall jet at one half of the rate of a round free jet. The momentum flux decreases fairly linearly in the three-dimensional wall jet due to the momentum lost to the wall, but at a significantly faster rate than for a two-dimensional wall jet.

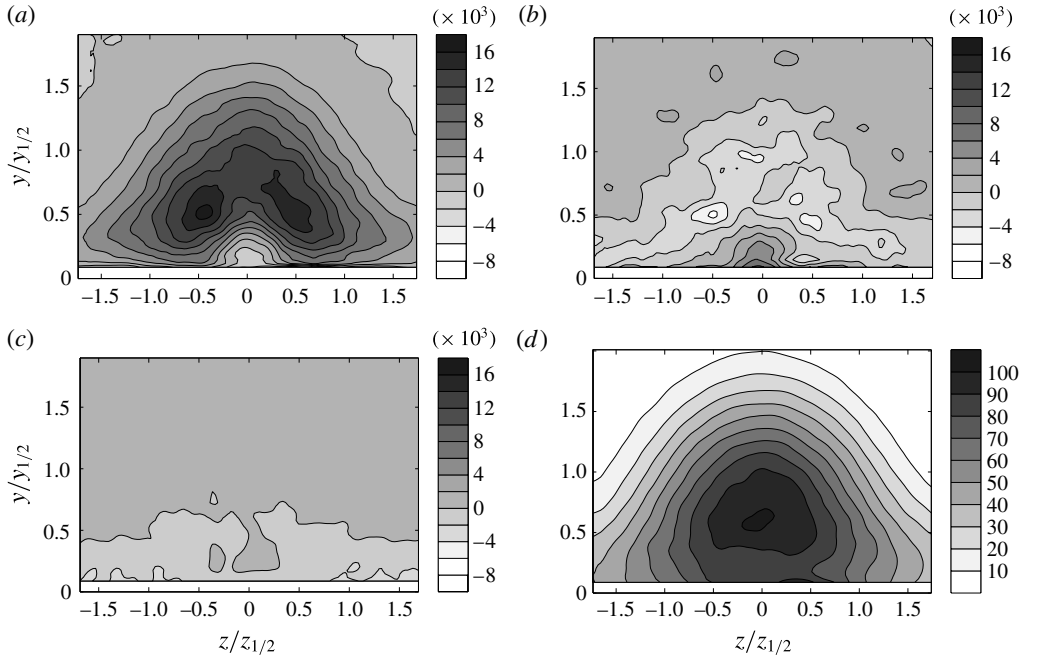

FIGURE 24. Contours of the turbulent kinetic energy budget at $x/D = 20$: (*a*) turbulent production, P (m^2 s^{-3}), (*b*) convection of turbulent energy by turbulence, $-((\partial\overline{qv}/\partial y) + (\partial\overline{qw}/\partial z))$ (m^2 s^{-3}), (*c*) convection of turbulent energy by mean, $(\overline{V}(\partial\overline{q}/\partial y) + \overline{W}(\partial\overline{q}/\partial z))$ (m^2 s^{-3}), and (*d*) turbulent kinetic energy, $(\overline{q})$ (m^2 s^{-2}).

For the first time, measurements of all six components of the Reynolds stresses were performed in the cross-flow plane of the three-dimensional wall jet. The distribution of the Reynolds stress field in the three-dimensional wall jet was compared at the jet centreline and across the jet at y_{max} for various streamwise locations. Throughout the jet, $\overline{u^2}$ makes the largest contribution to the Reynolds stress field. The measurement at the jet centreline indicates that both $\overline{uw}$ and $\overline{vw}$ are quite small compared with other Reynolds stresses; however, across the jet, $\overline{uw}$ is significantly larger than $\overline{vw}$. Typically, the magnitude of $\overline{w^2}$ is larger than that of $\overline{v^2}$, particularly near the wall in the far-field region, again illustrating that the turbulent anisotropy is an important feature of this flow, even far from the jet outlet.

The contours of $\overline{uv}$ show a large positive region with a maximum located around the vertical half-width and a smaller negative region close to the wall. As the flow evolved downstream, the negative region was suppressed down towards the wall and the outer positive region grew and diffused throughout the jet. The contours of $\overline{uw}$ have two regions with opposite sign, located on either side of the jet centreline, whereas the contours of $\overline{vw}$ indicate a pair of oppositely signed regions, one above the other, that are placed on either side of the jet centreline. However, the magnitude of $\overline{vw}$ was found to be quite small compared with other Reynolds stresses and, in fact, the relative contribution of this term decreases rapidly as the flow evolves downstream, and becomes difficult to distinguish in the far-field region because it is so small.

The distribution of the mean streamwise vorticity in the turbulent three-dimensional wall jet was examined at various streamwise locations. The contours of $\overline{\Omega}_x$ in the near field have a pair of counter-rotating regions that are located near the wall in the

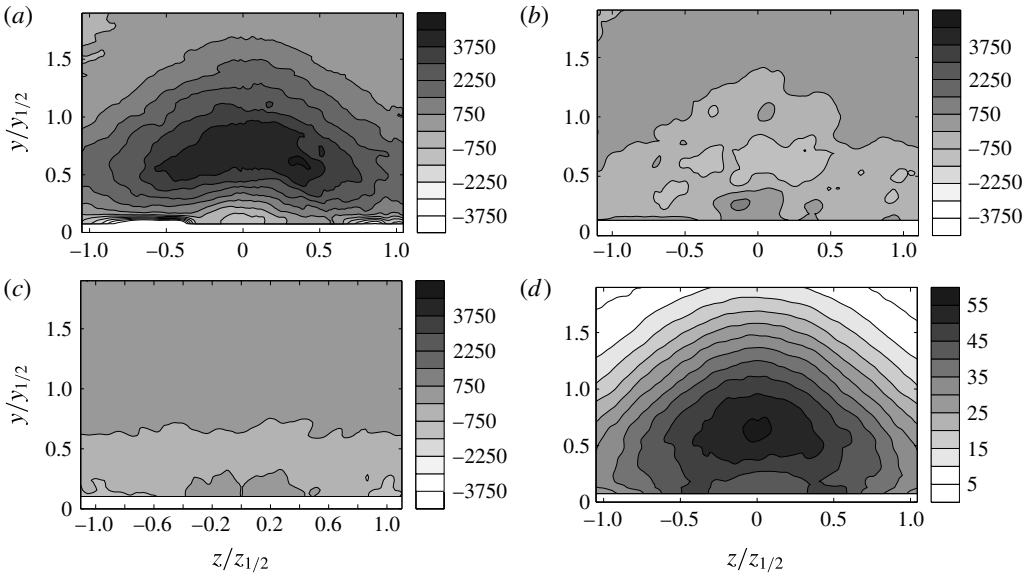

FIGURE 25. Contours of the turbulent kinetic energy budget at $x/D = 30$: (*a*) turbulent production, P (m^2 s^{-3}), (*b*) convection of turbulent energy by turbulence, $-((\partial\overline{qv}/\partial y) + (\partial\overline{qw}/\partial z))$ (m^2 s^{-3}), (*c*) convection of turbulent energy by mean, $(\overline{V}(\partial\overline{q}/\partial y) + \overline{W}(\partial\overline{q}/\partial z))$ (m^2 s^{-3}), and (*d*) turbulent kinetic energy, $(\overline{q})$ (m^2 s^{-2}).

lateral shear layers. As the flow evolves downstream, these regions begin to reorient themselves until the outer regions move above the inner regions. This causes the mean flow to be driven into the wall and laterally outward, thereby causing the large lateral growth of the three-dimensional wall jet.

The relative contributions from the difference in the Reynolds normal stresses, $(\overline{v^2} - \overline{w^2})$, and the Reynolds shear stress, $\overline{vw}$, were calculated and compared at each downstream location. At all locations, the magnitude of $(\overline{v^2} - \overline{w^2})$ is significantly larger than that of $\overline{vw}$, particularly near the wall. Furthermore, the gradients associated with the near-wall regions of $(\overline{v^2} - \overline{w^2})$ are oriented to reinforce the near-wall streamwise vorticity. Together, these results suggest that the anisotropy in the Reynolds normal stresses (term D) caused by the presence of the wall reinforces any vortex-line bending mechanism and contributes to the large lateral growth of the wall jet. Any turbulence model that hopes to capture the large lateral growth of the three-dimensional wall jet should be capable of capturing the anisotropy of the cross-flow normal stresses near the wall (experimental data can be found at supplementary data section).

Of the six turbulent kinetic energy production terms that could be computed here, the turbulent production terms corresponding to $-\overline{uv}(\partial\overline{U}/\partial y)$ and $-\overline{uw}(\partial\overline{U}/\partial z)$ were, by far, the largest contributors to the total production in the turbulent kinetic energy budget at all locations in the three-dimensional wall jet. As the jet evolved downstream, the contribution from the latter term diminished in proportion to the former. The results indicate that the majority of the turbulent energy is produced in the jet shear layers and near the wall. The turbulent transport term was negative in the outer shear-layer region, indicating that energy is diffusing from the shear layers; the regions inside and outside of the shear layers were positive, indicating

that turbulent kinetic energy diffuses into these regions. Even well downstream of the jet exit at $x/D = 20$ and 30, the results indicate that the turbulent energy budget obtained on the jet centreline is not fully indicative of the energy budgets off of the centreline.

Acknowledgements

The authors are grateful for the financial support of the Natural Sciences and Engineering Research Council of Canada, and Druk Green Power Corporation Limited of Bhutan.

Supplementary data

Supplementary data is available at https://www.researchgate.net/publication/303552765_Dataset_corresponding_to_Reynolds_Stress_Distribution_and_Turbulence_Generated_Secondary_Flow_in_the_Turbulent_Three-Dimensional_Wall_Jet_by_L_Namgyal_and_JW_Hall_Journal_of_Fluid_Mechanics_Accepted_2).

Appendix. Convection of turbulent kinetic energy by mean and fluctuating velocities

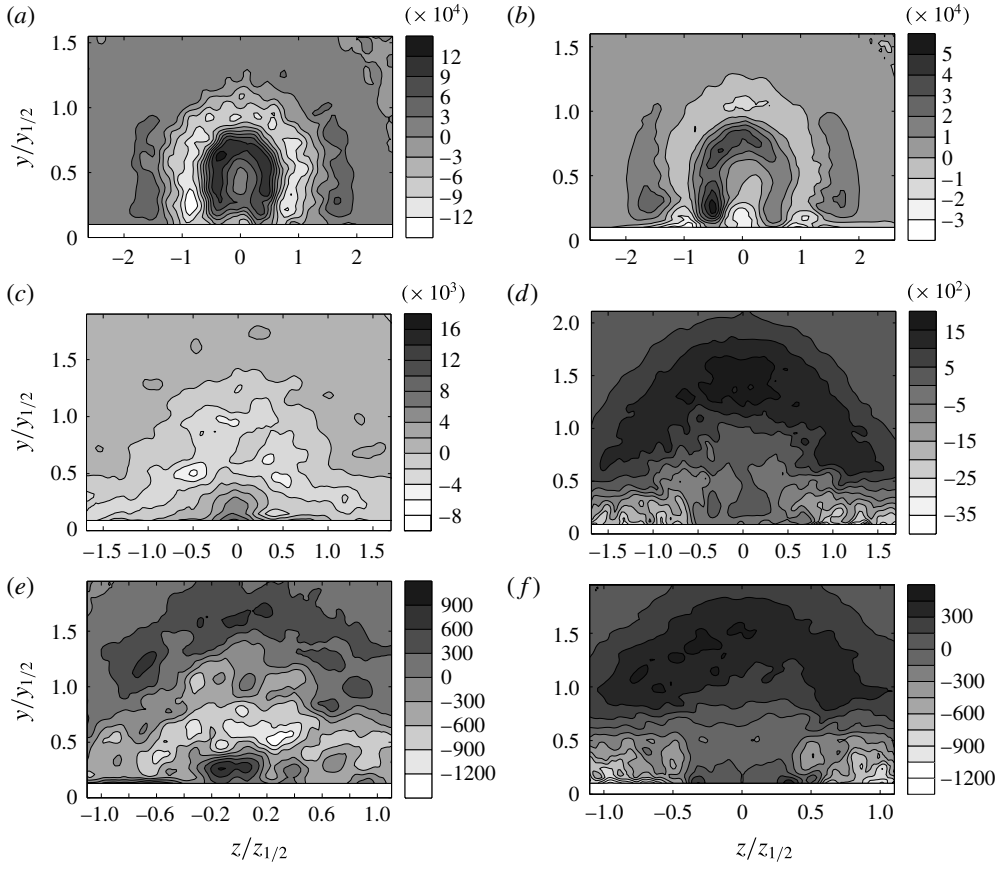

FIGURE 26. (a,c,e) Convection of turbulent energy by the fluctuating flow, $-((\partial\overline{qv}/\partial y) + (\partial\overline{qw}/\partial z))$ (m^2 s^{-3}), and (b,d,f) convection of turbulent energy by the mean flow, $(\overline{V}(\partial\overline{q}/\partial y) + \overline{W}(\partial\overline{q}/\partial z))$ (m^2 s^{-3}), at (a,b) $x/D = 5$, (c,d) $x/D = 20$, (e,f) $x/D = 30$.

REFERENCES

ABRAHAMSSON, H., JOHANSSON, B. & LOFDAHL, L. 1997*a* An investigation of the turbulence field in the fully developed three-dimensional wall jet. *Internal Rep.* 97-1. Chalmers University of Technology, Sweden.

ABRAHAMSSON, H., JOHANSSON, B. & LOFDAHL, L. 1997*b* The turbulence field of a fully developed three-dimensional wall jet. *Tech. Rep.* 91-1. Chalmers University of Technology, Sweden.

ADANE, K. F. K. & TACHIE, M. F. 2010 Experimental and numerical study of laminar round jet flows along a wall. *Trans. ASME J. Fluids Engng* **132**, 101203.

AGELINCHAAB, M. & TACHIE, M. F. 2011 Characteristics of turbulent three-dimensional wall jets. *J. Fluid Engng* **133** (2), 021201.

BRADSHAW, P. 1987 Turbulent secondary flow. *Annu. Rev. Fluid Mech.* **19**, 53–74.

BRUNDRETT, E. & BAINES, W. D. 1964 The production and diffusion of vorticity in duct flow. *J. Fluid Mech.* **19** (03), 375–394.

CAPP, S. P., HUSSIEN, H. J. & GEORGE, W. K 1990 Velocity measurements in a high Reynolds number, momentum-conserving, axisymmetric, turbulent jet. *Tech. Rep.* Turbulence Research Laboratory, University of Baffallo, SUNY.

COOPER, D., JACKSON, D. C., LAUNDER, B. E. & LIAU, G. X. 1993 Impinging jet studies for turbulence model assessment. I: flow-field experiments. *Intl J. Heat Mass Transfer* **36**, 2675–2684.

CRAFT, T. J. & LAUNDER, B. E. 2001 On the spreading mechanism of the three-dimensional turbulent wall jet. *J. Fluid Mech.* **435**, 305–326.

DAVIS, M. R. & WINARTO, H. 1980 Jet diffusion from a circular nozzle above a solid plane. *J. Fluid Mech.* **101**, 193–218.

ERIKSSON, J. G. & KARLSSON, R. I. 2000 Near-wall turbulence structure in the plane turbulent wall jet in still surroundings. In *10th International Symposium on Applications of Laser Techniques to Fluid Mechanics, Lisbon, Portugal*, Inst Superior Technico.

ERIKSSON, J. G., KARLSSON, R. I. & PERSSON, J. 1998 An experimental study of a two-dimensional plane wall jet. *Exp. Fluids* **25**, 50–60.

HALL, J. W. & EWING, D. 2005*a* The rectangular wall jet. Part I: the effect of varying aspect ratio. In *43rd AIAA Aerospace Sciences Meeting and Exhibit, 10–13 Jan 2005, Reno, Nevada. AIAA Paper* 2005-0115.

HALL, J. W. & EWING, D. 2005*b* The rectangular wall jet. Part II: role of the large-scale structures. In *43rd AIAA Aerospace Sciences Meeting and Exhibit, 10–13 Jan 2005, Reno, Nevada. AIAA Paper* 2005-0116.

HALL, J. W. & EWING, D. 2006 A combined spatial and temporal decomposition of the coherent structures in the three-dimensional wall jet. In *44th AIAA Aerospace Sciences Meeting and Exhibit, 9–12 Jan 2006, Reno, Nevada. AIAA Paper* 2006-308.

HALL, J. W. & EWING, D. 2007*a* The asymmetry of the large-scale structures in turbulent three-dimensional wall jets exiting long rectangular channels. *Trans. ASME J. Fluids Engng* **129**, 929–941.

HALL, J. W. & EWING, D. 2007*b* The development of three-dimensional turbulent wall jets issuing from moderate aspect ratio rectangular channels. *AIAA J.* **45** (6), 1177–1186.

HALL, J. W. & EWING, D. 2010 Spectral linear stochastic estimation of the turbulent velocity in a square three-dimensional wall jet. *Trans. ASME J. Fluids Engng* **132** (5).

HUSSEIN, H. J., CAPP, S. P. & GEORGE, W. K. 1994 Velocity measurements in a high-Reynolds-number momentum-conserving axisymmetric turbulent jet. *J. Fluid Mech.* **258**, 31–75.

LAUNDER, B. E. & RODI, W. 1983 The turbulent wall jet – measurements and modelling. *Annu. Rev. Fluid Mech.* **15**, 429–459.

LAVISION 2007 *Product Manual – Flow Master*. LaVision GmbH.

MATHIEU, J. & SCOTT, J. 2000 *An Introduction to Turbulent Flow*. Cambridge University Press.

MATSUDA, H., IIDA, S. & HAYAKAWA, M. 1990 Coherent structures in three-dimensional wall jet. *Trans. ASME J. Fluids Engng* **112**, 462–467.

NAMGYAL, L. 2012 Three-component particle image velocimetry measurements in a turbulent three-dimensional wall jet. PhD thesis, University of New Brunswick, Fredericton, New Brunswick, Canada.

NAMGYAL, L. & HALL, J. W. 2010 PIV measurements of the turbulent secondary flow in a three-dimensional wall jet. In *Proceedings of ASME 2010 3rd Joint US–Engineering Summer Meeting and 8th International Conference on Nanochannels, Microchannels & Minichannels. Montreal, Canada*, ASME, Paper Number FEDSM–ICNMM2010-30278.

NAMGYAL, L. & HALL, J. W. 2011 A POD investigation of the three-dimensional wall jet near field. In *Seventh International Symposium on Turbulence and Shear Flow Phenomena (TSFP-7), Ottawa, Canada*. Taylor & Francis.

PADMANABHAM, G. & GOWDA, B. H. L. 1991*a* Mean and turbulence characteristics of a class of three-dimensional wall jets. Part 1: mean flow characteristics. *Trans. ASME J. Fluids Engng* **113**, 620–628.

PADMANABHAM, G. & GOWDA, B. H. L. 1991*b* Mean and turbulence characteristics of a class of three-dimensional wall jets. Part 2: turbulence characteristics. *Trans. ASME J. Fluids Engng* **113**, 620–628.

PANCHAPAKESAN, N. R. & LUMLEY, J. L. 1993 Turbulence measurement in axisymmetric jets of air and helium. Part 1: air jet. *J. Fluid Mech.* **246**, 197–223.

QUINN, W. R. 2005 Measurements in the near field of an isosceles triangular turbulent free jet. *Experiments* **39** (1), 111–126.

RAJARATNAM, N. & PANI, B. S. 1974 Three-dimensional turbulent wall jets. *J. Hydraul. Div. ASCE* **100**, 69–83.

ROSTAMY, N., BERGSTROM, D. J., SUMNER, D. & BUGG, J. D. 2011 The effect of surface roughness on the turbulence structure of a plane wall jet. *Phys. Fluids* **23** (8), 085103.

SUN, H. 2002 The effect of initial conditions on the development of the three-dimensional wall jet. PhD thesis, McMaster University, Hamilton, Ontario, Canada.

SUN, H. & EWING, D. 2002*a* Development of the large-scale structures in the intermediate region of the three-dimensional wall jet. In *Proceedings of the Fluids Engineering Division Summer Meeting Montreal, New York*, ASME, Paper Number FEDSM2002-31414.

SUN, H. & EWING, D. 2002*b* Effect of initial and boundary conditions on the development of three-dimensional wall jet. In *Proceedings of the AIAA winter meeting, Tahoe*.

TACHIE, M. F. 2000 Open channel turbulent boundary layers and wall jets on rough surfaces. PhD thesis, University of Saskatchewan.

TINNEY, C. E., GLAUSER, M. N. & UKEILEY, L. S. 2008 Low-dimensional characteristics of a transonic jet. Part 1: proper orthogonal decomposition. *J. Fluid Mech.* **612**, 107–141.

VENAS, B., ABRAHAMSSON, H., KROGSAD, P. A. & LOFDAHL, L. 1999 Pulsed hot-wire measurements in two and three-dimensional wall jets. *Exp. Fluids* **27**, 210–218.

WHITTAKER, E. T. 1915 On the functions which are represented by the expansion of the interpolation-theory. *Proc. R. Soc. Edin.* **35**, 181–194.

WYGNANSKI, I. & FIEDLER, H. 1969 Some measurements in the self-preserving jet. *J. Fluid Mech.* **38**, 577–612.

XU, H. 2009 Direct numerical simulation of turbulence in a square duct. *J. Fluid Mech.* **621**, 23–57.